Combustion and Flame 160 (2013) 995–1011

Contents lists available at SciVerse ScienceDirect

Combustion and Flame

journal homepage: www.elsevier.com/locate/combustflame

An experimental and detailed chemical kinetic modeling study of hydrogen and syngas mixture oxidation at elevated pressures

Alan Kéromnès [a,*], Wayne K. Metcalfe [a], Karl A. Heufer [a], Nicola Donohoe [a], Apurba K. Das [b,c], Chih-Jen Sung [c], Jürgen Herzler [d], Clemens Naumann [d], Peter Griebel [d], Olivier Mathieu [e], Michael C. Krejci [e], Eric L. Petersen [e], William J. Pitz [f], Henry J. Curran [a]

[a] Combustion Chemistry Centre, National University of Ireland, Galway, University Rd., Galway, Ireland
[b] Case Western Reserve University, Department of Mechanical & Aerospace Engineering, Cleveland, OH 44106, USA
[c] University of Connecticut, Department of Mechanical Engineering, Storrs, CT 06269, USA
[d] German Aerospace Center (DLR), Institute of Combustion Technology, Stuttgart, Germany
[e] Texas A & M University, Department of Mechanical Engineering, College Station, TX 77843, USA
[f] Lawrence Livermore National Laboratory, Livermore, CA 94551, USA

ARTICLE INFO

Article history:
Received 8 June 2012
Received in revised form 24 October 2012
Accepted 7 January 2013
Available online 12 March 2013

Keywords:
Hydrogen
Syngas
Kinetic mechanism
Ignition delay times
Flame speed

ABSTRACT

The oxidation of syngas mixtures was investigated experimentally and simulated with an updated chemical kinetic model. Ignition delay times for $H_2/CO/O_2/N_2/Ar$ mixtures have been measured using two rapid compression machines and shock tubes at pressures from 1 to 70 bar, over a temperature range of 914–2220 K and at equivalence ratios from 0.1 to 4.0. Results show a strong dependence of ignition times on temperature and pressure at the end of the compression; ignition delays decrease with increasing temperature, pressure, and equivalence ratio. The reactivity of the syngas mixtures was found to be governed by hydrogen chemistry for CO concentrations lower than 50% in the fuel mixture. For higher CO concentrations, an inhibiting effect of CO was observed. Flame speeds were measured in helium for syngas mixtures with a high CO content and at elevated pressures of 5 and 10 atm using the spherically expanding flame method. A detailed chemical kinetic mechanism for hydrogen and H_2/CO (syngas) mixtures has been updated, rate constants have been adjusted to reflect new experimental information obtained at high pressures and new rate constant values recently published in the literature. Experimental results for ignition delay times and flame speeds have been compared with predictions using our newly revised chemical kinetic mechanism, and good agreement was observed. In the mechanism validation, particular emphasis is placed on predicting experimental data at high pressures (up to 70 bar) and intermediate- to high-temperature conditions, particularly important for applications in internal combustion engines and gas turbines. The reaction sequence $H_2 + H\dot{O}_2 \leftrightarrow \dot{H} + H_2O_2$ followed by $H_2O_2\ (+M) \leftrightarrow \dot{O}H + \dot{O}H\ (+M)$ was found to play a key role in hydrogen ignition under high-pressure and intermediate-temperature conditions. The rate constant for $H_2 + H\dot{O}_2$ showed strong sensitivity to high-pressure ignition times and has considerable uncertainty, based on literature values. A rate constant for this reaction is recommended based on available literature values and on our mechanism validation.

1. Introduction

Hydrogen has attracted a lot of attention as a transportation fuel because of its low greenhouse gas emissions compared to carbon-based fuels. Although most current research is focused on using hydrogen in fuel cells, hydrogen can also be used with high efficiency in internal combustion (IC) engines to power transportation vehicles [1]. Hydrogen has drawn recent attention because, by using argon instead of nitrogen as a bath gas, higher efficiencies have been obtained in hydrogen engines [2,3]. Syngas (H_2 and CO mixtures) has also been a focus of recent interest because it can be derived from the gasification of biomass and used for efficient power production in stationary gas turbines (GT) and engines. To design new engines, computational fluid dynamics (CFD) models are needed to simulate hydrogen and syngas combustion in IC engines and predict optimal engine design, operating conditions, and performance. These CFD models need an accurate hydrogen/syngas chemical kinetics submodel to predict the rate of reaction of this fuel under engine-relevant conditions. Many chemical kinetics models in the literature rely on detailed

* Corresponding author. Current address: Institut Supérieur de l'Automobile et des Transports (ISAT) DRIVE Laboratory, University of Burgundy, 49 rue Mlle Bourgeois, 58027 Nevers, France.
E-mail address: alan.keromnes@u-bourgogne.fr (A. Kéromnès).

0010-2180/$ - see front matter © 2013 The Combustion Institute. Published by Elsevier Inc. All rights reserved.
http://dx.doi.org/10.1016/j.combustflame.2013.01.001

chemistry for hydrogen [3–9] and syngas [10–12]. However, fuel–air mixtures in an IC engine are subjected to higher pressures and temperatures than found in typical experimental setups for combustion studies. The syngas chemical kinetic mechanisms that are available in the literature have not been extensively validated at such high pressures and temperatures. Indeed, in 2006 Mittal et al. [13] stated that further refinements are still needed in the H_2/O_2 mechanism at high pressure and at intermediate temperature to achieve good agreement with their ignition data from a rapid compression machine (RCM).

Only a few experimental studies of hydrogen and syngas have been performed at high pressures and relatively low temperatures ($\leqslant$1000 K). The hydrogen autoignition process was studied by Lee and Hochgreb [14] in an RCM over a pressure range of 6–40 bar, in the temperature range 950–1050 K, using a stoichiometric mixture diluted in argon.

Recently, new experimental data has become available that extend the validation of hydrogen mechanisms to high pressures. Bradley et al. [15] and Burke et al. [16] have measured the laminar flame speed of hydrogen–air mixtures at elevated pressures up to 25 bar. Mittal and Sung [13] measured ignition delay times of hydrogen–air mixtures in a rapid compression machine at pressures up to 50 bar. Gersen et al. [17] studied the autoignition of hydrogen under conditions similar to those investigated by Lee and Hochgreb and Mittal et al. and found good agreement with the previous studies.

New experimental data has also become available to validate the syngas chemical kinetic mechanism. Mittal et al. [13] also used an RCM to measure ignition delays of syngas mixtures (from pure hydrogen to 80% CO + 20% H_2) diluted mainly in argon over the same temperature range (950–1050 K) at end-of-compression pressures of 15, 30, and 50 bar. Their results agreed with the previous experiments of Lee and Hochgreb [14]. Walton et al. [18] studied the same type of mixture but used nitrogen as the diluent over a pressure and temperature range of 7.1–26.4 atm and 855–1051 K, respectively. Despite the experimental conditions being somewhat different, they found good agreement with previous studies.

In this study, new hydrogen and syngas oxidation data have been acquired. Ignition delay times have been measured in rapid compression machines and shock tubes at pressures from 1 to 70 bar over a temperature range of 900–2500 K and at equivalence ratios from 0.1 to 4.0. The impact of the CO concentration on mixture oxidation behavior has been investigated for fuel mixtures over the range from pure hydrogen to fuel mixtures with 95% CO.

Flame speed measurements have been performed in helium for syngas mixtures with a high CO content (95%) over an equivalence ratio range of 0.5–3.5 and at pressures of 5 and 10 atm. Experimental results are finally compared to our newly revised chemical kinetic mechanism.

Using this experimental dataset extended to conditions of higher pressure and temperature, we have revalidated our chemical kinetic mechanism for H_2 and H_2/CO mixtures.

In the following sections, we describe the detailed chemical kinetic mechanism, present model validation comparisons and provide chemical kinetic insights into the behavior of hydrogen and syngas at pressures and temperatures characteristic of IC engines.

2. Numerical model

2.1. Flame speed

Chemkin Pro [20] was used to perform flame speed calculations. In preliminary flame calculations, we investigated the effect of the choice of Chemkin transport options on the computed flame speed. As a reference case, we used the Middha et al. [21,22] baseline condition of a stoichiometric hydrogen–air mixture at one atmosphere and an unburned gas temperature of 300 K. The transport options tested included mixture-averaged, multi-component, and thermal diffusion options. The multi-component transport model is more accurate than the mixture-averaged one. When thermal diffusion was included, the flame speed decreased by up to 8% for stoichiometric mixtures ($\phi = 1.0$) and 4% at $\phi = 2.5$. This was the biggest effect found when differences in the choice of transport options were selected. For all of the flame speed results presented below, we used the multi-component and thermal diffusion options. Next, we investigated the number of grid points in the one-dimensional mesh needed for an accurate flame speed calculation. As the number of grid points was increased, the flame speed converged close to the value with 400 grid points. To be conservative, Chemkin convergence parameters were adjusted so that at least 800 grid points (and at times as many as 1000) were used in the calculations in this study.

2.2. Rapid compression machine

The ignition delay time simulations of the RCM use a volume profile generated from the corresponding nonreactive pressure trace, for which an experiment is performed by replacing oxygen with nitrogen in the fuel–"air" charge. The volume history used for the simulation included the heat loss during the compression stroke by adding an empirically determined additional volume, and the heat loss after the end of compression was accounted for by the "adiabatic core expansion" approach [23]. The volume history is then used as an input in the Chemkin input file.

2.3. Shock tube

Shock tube data were simulated using constant-volume adiabatic conditions with the reflected shock pressure and temperature used as the initial conditions.

For long ignition delay times at lower temperatures in the DLR shock-tube, a gas-dynamic effect appears, which slightly increases both the pressure and the temperature. The pressure and temperature variations due to the gas dynamics of the shock tube behind reflected shock waves are considered in the simulations by using an MPFR (multiple plug flow reactor), an extension to CHEMKIN II [19]. This program, developed at DLR Stuttgart, takes into account gas-dynamic effects causing pressure and temperature variations decoupled from the effects of heat release by chemical reactions combined with pressure relaxation effects along the shock propagation direction due to the shock tube's "open end" configuration. Thus, the simulation assumes for a time period of typically 25 μs or shorter, depending on the temperature increase due to heat release ($\Delta T/T \leqslant 0.5\%$), a PFR with constant-pressure conditions and takes into account the propagation of the pressure increase by heat release within a PFR time-step along the propagation direction of the reflected shock. The correction of the gas dynamic effects is based on measured pressure histories of mixtures with similar acoustic properties but without heat release by chemical reactions or of mixtures with very long ignition delay times and no heat release before ignition (see Fig. S1 in the Supplementary Material). The temperature profiles are then calculated by applying adiabatic and isentropic conditions. These temperature profiles are used instead of constant initial temperatures T_5 for the simulation of the experiments. Thus, temperature variations are caused both by the gas dynamics and by the heat release of the reactive system.

2.4. Jet-stirred and variable-pressure-flow reactors

Predicted species profiles have been compared to experimental species profiles from a jet-stirred reactor (JSR) and a variable-

pressure-flow reactor (VPFR). The JSR is simulated using the Aurora package in Chemkin Pro assuming a constant-volume, homogeneous open reactor and assuming constant temperature, pressure, and residence time in the reactor. The convergence criterion is based on the change in species concentration. The VPFR is modeled using the Aurora package from Chemkin Pro assuming a constant-pressure reactor. The initial conditions are defined by the initial experimental conditions. However, the model assumes perfect and instantaneous mixing of the reactants, which is not the case during the experiments. Therefore, the time at which reaction starts in the experiments is not well defined, and it is reasonable to shift the predicted species profiles relative to the measured profiles to account for nonidealities in reaction initiation. This profile is shifted in time so that the predicted point corresponding to 50% of the fuel disappearance matches that reported experimentally.

3. Chemical kinetic mechanism

Several reactions have been identified in the literature as being important for hydrogen and syngas oxidation. Previous studies of hydrogen [4–6,10] have shown that its reactivity is mainly controlled by the competition between the chain-branching reaction

$$\dot{H} + O_2 \leftrightarrow \ddot{O} + \dot{O}H \qquad (R1)$$

and the pressure-dependent chain-propagating reaction

$$\dot{H} + O_2(+M) \leftrightarrow H\dot{O}_2(+M). \qquad (R9)$$

Therefore, these two reactions have been studied extensively [24–29]. For high-pressure conditions, the thermal decomposition of hydrogen peroxide (H_2O_2) via the pressure-dependent reaction

$$H_2O_2(+M) \leftrightarrow \dot{O}H + \dot{O}H(+M) \qquad (R15)$$

becomes the dominant chain-branching reaction. Finally, as for most fuels, at intermediate temperatures, the reaction between the fuel and $H\dot{O}_2$

$$H_2 + H\dot{O}_2 \leftrightarrow H_2O_2 + \dot{H}, \qquad (R17)$$

is important in the prediction of accurate ignition delay times.

Figure 1 shows the ignition behavior in low-, intermediate-, and high-temperature regions for 8, 16, and 32 bar. The figure also gives reactions that control the ignition behavior in each temperature region. Under low- to intermediate-temperature conditions (in the temperature range investigated in RCMs), hydrogen oxidation is governed by R9, which leads to the production of $H\dot{O}_2$ radicals. The hydroperoxyl radical reacts with H_2, leading to the formation of H_2O_2, which decomposes into two $\dot{O}H$ radicals. At higher temperatures (in the temperature range investigated in shock tubes), the competition between R1 and R9 leads to an unusual pressure dependence of the ignition delay times. Depending on the pressure, at higher temperatures the oxidation process is mainly governed by R1. Due to the pressure dependence of reaction R9, the temperature range in which the competition between R1 and R9 occurs depends on the pressure.

3.1. Sensitivity analysis

In this section, a sensitivity analysis of the reaction mechanism is presented to show the important reactions that should be highlighted in the following discussion of the mechanism development. The sensitivity analysis has been performed with the present mechanism. The effect of the reaction rate constants on ignition delay times and flame speeds was examined. The analysis was performed over a wide range of pressures (1–100 bar) and temperatures (850–1200 K) for ignition delay times (Figs. 2 and S2 in the Supplementary Material). Each reaction is increased and decreased by a factor of 2 in calculating the ignition time. The sensitivity coefficient (σ) is calculated by Eq. (1), where τ' and τ'' are the calculated ignition times with the reaction increased and decreased, respectively. This analysis is performed assuming ideal (constant volume and adiabatic) conditions:

$$\sigma = \frac{\log\left(\frac{\tau'}{\tau''}\right)}{\log\left(\frac{2.0}{0.5}\right)}. \qquad (1)$$

For the case of hydrogen, the sensitivity analysis shows that, at low temperature (below 1000 K) and at relatively low pressure (1 atm), the reactivity is mainly controlled by the competition between the chain-branching reaction R1 and the chain-terminating reaction R9 (Fig. S2 in the Supplementary Material). However, at higher temperatures ($T > 1000$ K), the reactivity is only controlled by the chain-branching reaction. Under high-pressure and intermediate-temperature conditions, Fig. 2, the reactivity is mainly controlled by the reactions producing and consuming H_2O_2, R15 and R17. This reaction sequence of fuel reacting with $H\dot{O}_2$ radicals to make H_2O_2, which subsequently decomposes to produce two $\dot{O}H$ radicals, leading to chain branching, was first identified by Pitz and

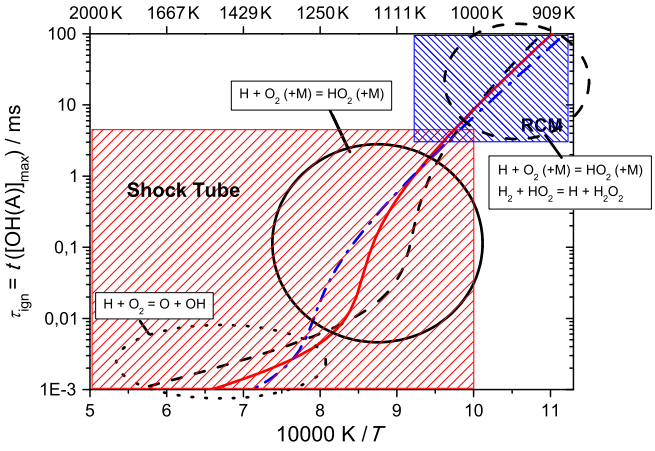

Fig. 1. Main reactions as functions of the temperature regime for a mixture of 0.7 H_2 + O_2 + 3.76 Ar tested with the present mechanism at 8 bar (---), 16 bar (——) and 32 bar (— · —). (For interpretation of the references to color in this figure legend, the reader is referred to the web version of this article.)

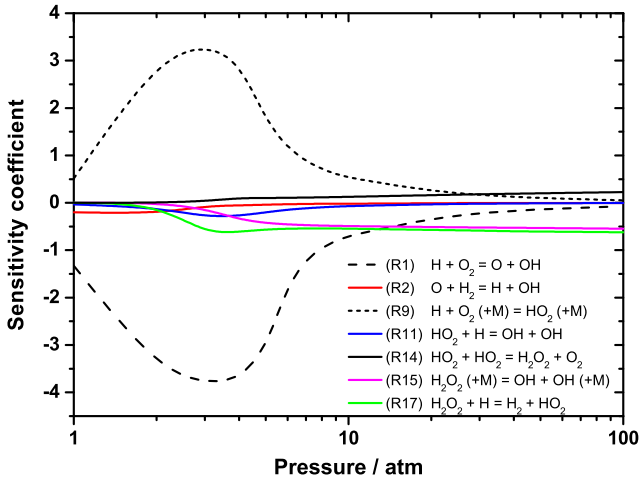

Fig. 2. Sensitivity analysis of ignition time delays as a function of pressure at 1000 K for the present mechanism (mixture: $H_2/O_2/N_2/Ar$ = 1/1/1.88/1.88). Only the seven most sensitive reactions are included, for clarity.

Westbrook [30]. These reactions are counter-balanced by the increasing sensitivity with pressure to the chain-terminating reaction:

$$H\dot{O}_2 + H\dot{O}_2 \leftrightarrow H_2O_2 + O_2. \quad (R14)$$

The sensitivity analysis for flame speed was performed using Chemkin Pro. The sensitivity analysis is with respect to mass flow rate, which is directly proportional to flame speed. It was performed for hydrogen in air at room temperature and pressure and for a range of stoichiometries from 0.5 to 2.0 (Fig. 3). The flame speeds under these conditions are controlled by the previously identified reactions R1 and R9, but other reactions also play a key role:

$$\ddot{O} + H_2 \leftrightarrow \dot{H} + \dot{O}H \quad (R2)$$

$$\dot{O}H + H_2 \leftrightarrow \dot{H} + H_2O \quad (R3)$$

$$H\dot{O}_2 + \dot{H} \leftrightarrow \dot{O}H + \dot{O}H \quad (R11)$$

$$H\dot{O}_2 + \dot{O}H \leftrightarrow H_2O + O_2. \quad (R13)$$

It is evident that laminar flame speed is mainly controlled by the production and consumption of $\dot{H}$ atoms. The chain-terminating reaction forming water via

$$\dot{H} + \dot{O}H + M \leftrightarrow H_2O + M \quad (R8)$$

is also important, and increasing its rate constant reduces reactivity. Moreover, it has to be noted that R9 decreases flame reactivity under very lean conditions ($\phi \leqslant 0.7$) but increases the reactivity of stoichiometric and rich mixtures. This is due to the competition between R11 and R13. Under lean conditions, there are fewer $\dot{H}$ atoms available and the $H\dot{O}_2$ radical consumes the $\dot{O}H$ radical to form water and molecular oxygen, whereas, under stoichiometric and rich conditions, the $H\dot{O}_2$ radical can react with $\dot{H}$ atoms to produce $\dot{O}H$ radicals, R11. Therefore, we have paid particular attention to these reactions in updating the mechanism previously published by Ó Conaire et al. [4].

For the case of syngas, a sensitivity analysis was performed based on the mixture with the higher CO concentration tested by Mittal et al. [13] at three different end-of-compression pressures (15, 30 and 50 bar) at 1000 K. Only the 15 most sensitive reactions have been plotted (Fig. 4). Only four reactions involving CO appear to be important in this system dominated by hydrogen chemistry:

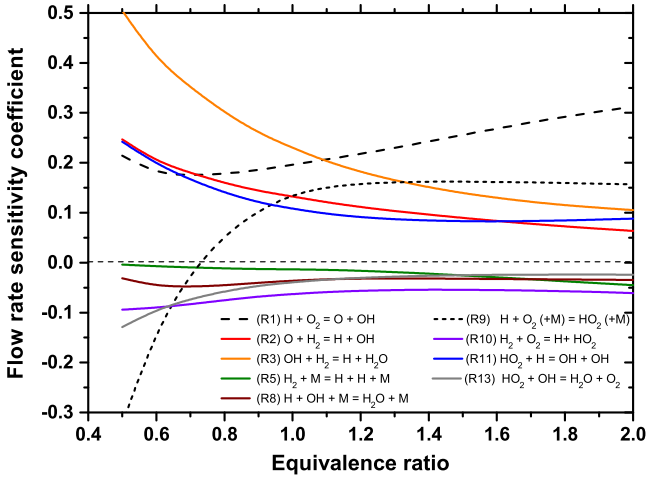

Fig. 3. Flow rate sensitivity analysis of laminar flame speed of hydrogen in air at 298 K and 1 atm as a function of equivalence ratio for the present mechanism. Only the nine most sensitive reactions are included, for clarity.

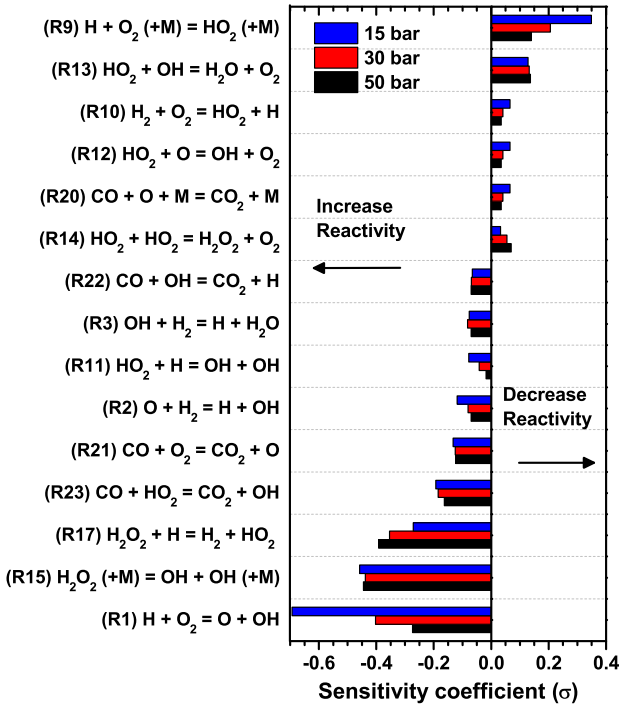

Fig. 4. The 15 most sensitive reactions at 1000 K and pressures of 15, 30, and 50 bar. Mixture: $H_2/CO/O_2/N_2/Ar = 2.5/10/6.25/18.125/63.125$.

$$CO + \ddot{O} + M \leftrightarrow CO_2 + M \quad (R20)$$

$$CO + O_2 \leftrightarrow CO_2 + \ddot{O} \quad (R21)$$

$$CO + \dot{O}H \leftrightarrow CO_2 + \dot{H} \quad (R22)$$

$$CO + H\dot{O}_2 \leftrightarrow CO_2 + \dot{O}H. \quad (R23)$$

Particular attention has been paid to these four reactions, and these will be discussed below.

3.2. Development of the hydrogen mechanism

The detailed chemical kinetic mechanism of hydrogen is based on our earlier hydrogen mechanism [4]. Rate constants for reactions were updated to reflect more accurate values now available from measurements and calculations in the literature. The hydrogen experiments of Mittal et al. [13] were used as a benchmark to assess the performance of the hydrogen mechanism. The performance of the ignition delay time prediction is evaluated when it is updated with the recently published rate constant measurements. This evaluation has been performed through four main steps, which are presented in Fig. 5. These steps are as follows. Figure 5a presents the influence of the reaction rate for reactions R1 and R17. This results in the intermediate mechanism called "step 1." Figure 5b presents the impact of the reaction rate for first pressure-dependent reaction R9 and results in the second intermediate mechanism, called "step 2." In Fig. 5c, the impact of two recent recommendations for the pressure dependent reaction R15 is assessed. Our recommendation results in the third intermediate mechanism called "step 3." Finally, Fig. 5d presents the performance of the present mechanism against the experimental results from Mittal et al. [13]. For the ignition calculations in a rapid compression machine, a special subroutine from Case Western Reserve University (CWRU) was used to simulate the volume history and heat losses in the machine.

The reactions and associated rate constants for the H_2/CO mechanism are provided in Tables 1 and 2. The thermodynamic values

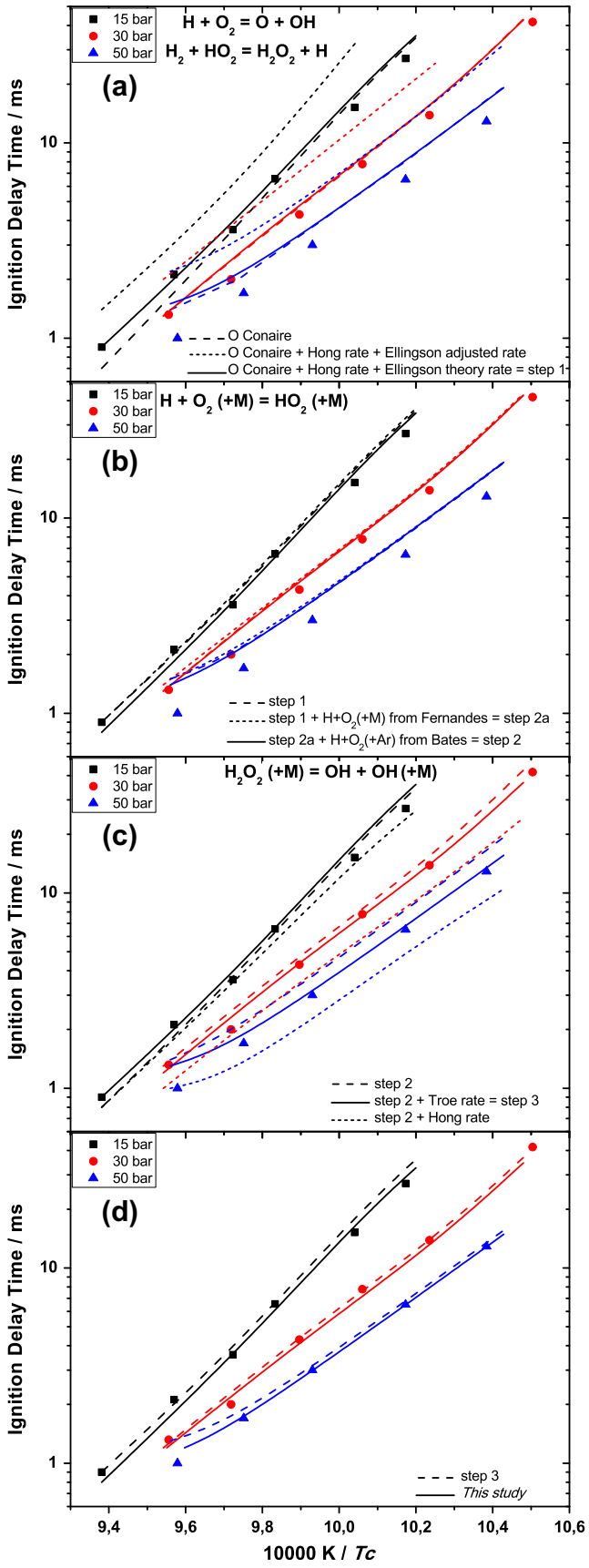

Fig. 5. Main steps for the kinetic mechanism improvement. Experimental results: Mittal et al. [13].

used for species are given in the Supplementary Material (Table S1). The enthalpy of formation of ȮH radicals is from the recent work of Ruscic et al. [31]. The enthalpy of formation for $H\dot{O}_2$ (2.94 kcal/mol) is from Burcat's and Ruscic's database [32].

3.2.1. $\dot{H} + O_2 \leftrightarrow \ddot{O} + \dot{O}H$ *(R1)*

The reaction R1 not only is extremely important in the hydrogen sub-mechanism (Figs. 2, 3, and S2) but also dominates/controls the oxidation of all fuels undergoing oxidation at high temperature ($T \geqslant 1000$ K, depending on the pressure). At temperatures below approximately 1000 K, this reaction competes with the propagation reaction R9, which is inhibiting, as it produces only one radical and not two reactive radicals, as in the chain-branching reaction. We have adopted the recently measured rate constant for R1 from Hong et al. [25]. They measured H_2O absorption behind reflected shock waves at 2 atm over a tempereture range of 1100–1530 K. They combined their results with those previously reported by Masten et al. [29] over a temperature range of 1450–3370 K and found very good agreement in the overlapping temperature range. Based on these two datasets, a rate constant was determined over a temperature range of 1100–3370 K with a reduced uncertainty of less than 10% over this temperature range. The rate constant is also in good agreement with the experimental results from Pirraglia et al. [33] and is used in recently published hydrogen mechanisms [6,9].

This value is lower than our previous recommendation, taken from the work of Hessler [34], and results in the prediction of slightly longer ignition times at intermediate temperatures and low pressures and slightly shorter ignition delay times at higher pressures (Fig. 5a).

3.2.2. $H_2 + H\dot{O}_2 \leftrightarrow H_2O_2 + \dot{H}$ *(R17)*

This reaction was found to exhibit a high sensitivity at the high pressures and low temperatures found in the RCM experiments (Fig. 2). At 1000 K, the recommended rate constant from Baulch et al. [35] is a factor of 3 lower than Tsang and Hampson's recommendation [36]. A comparison of the different rate constants is given in the Supplementary Material (Fig. S3). Based on the sensitivity results, this would result in a factor of 3 difference in ignition delay time at 1000 K and 50 bar. Ellingson et al. [37] recently used ab initio methods to compute the rate constant. They used canonical variational transition state theory with multidimensional tunneling (CVT/SCT) for the reverse reaction which leads to $H_2 + H\dot{O}_2$ and $H_2O + \dot{O}H$. Their calculation is similar to Tsang's recommendation below 1000 K and results in ignition delay time predictions that are much more consistent with Mittal and Sung's measurements. However, the ab initio rate constant was too fast, compared to experimental data from Baldwin et al. [38], and so Ellingson et al. adjusted the barrier height to the upper theoretical limit in order to reduce the rate constant and match Baldwin's experimental data. Unfortunately, in the RCM experiments, this adjustment results in a decreased reactivity and the model reproduces the RCM ignition delay data more precisely (Fig. 5a) when the unaltered theoretical rate constant is used. Therefore, the unaltered theoretical reaction rate constant calculated by Ellingson et al. [37] is used in the present study.

3.2.3. *Pressure-dependent reactions (R9 and R15)*

The reactivity of hydrogen is highly sensitive to the pressure-dependent reactions R9 and R15 in the low- to intermediate-temperature regime. At 1000 K and low to intermediate pressure (below 10 atm), R9 controls the reactivity, whereas, at higher pressures and over the same temperature range, the reactivity is mainly controlled by R15 (Fig. 2).

Table 1
Detailed H_2–CO reaction mechanism (units: cm^3/mol/s/cal).

#	Reaction	A	n	E_A	Ref.
1	$H + O_2 = O + OH$	1.040E+14	0.00	1.529E+04	[25]
2	$O + H_2 = H + OH$	5.080E+04	2.67	6.292E+03	[90]
3	$OH + H_2 = H + H_2O$	4.380E+13	0.00	6.990E+03	[47]
4	$O + H_2O = OH + OH$	2.970E+06	2.02	1.340E+04	[91]
5	$H_2 + M = H + H + M$	4.577E+19	−1.40	1.044E+05	[36]
	$\varepsilon_{H_2} = 2.5,\ \varepsilon_{H_2O} = 12,\ \varepsilon_{CO} = 1.9,\ \varepsilon_{CO_2} = 3.8,\ \varepsilon_{He} = 0.83$				
6	$O + O + M = O_2 + M$	6.165E+15	−0.50	0.00	[36]
	$\varepsilon_{H_2} = 2.5,\ \varepsilon_{H_2O} = 12,\ \varepsilon_{CO} = 1.9,\ \varepsilon_{CO_2} = 3.8,\ \varepsilon_{Ar} = 0.83,\ \varepsilon_{He} = 0.83$				
7	$O + H + M = OH + M$	4.714E+18	−1.00	0.00	[36]
	$\varepsilon_{H_2} = 2.5,\ \varepsilon_{H_2O} = 12,\ \varepsilon_{CO} = 1.5,\ \varepsilon_{CO_2} = 2.0,\ \varepsilon_{Ar} = 0.75,\ \varepsilon_{He} = 0.75$				
8	$H + OH + M = H_2O + M$	3.500E+22	−2.00	0.00	[7] × 0.92
	$\varepsilon_{H_2} = 0.73,\ \varepsilon_{H_2O} = 3.65,\ \varepsilon_{Ar} = 0.38,\ \varepsilon_{He} = 0.38,\ \varepsilon_{CO} = 1.9,\ \varepsilon_{CO_2} = 3.8$				
9	$H + O_2 (+M) = HO_2 (+M)$[a]	4.65E+12	0.44	0.00	[24]
	Low-pressure limit	1.737E+19	−1.23	0.00	[24]
	$\varepsilon_{H_2} = 1.3,\ \varepsilon_{H_2O} = 10,\ \varepsilon_{CO} = 1.9,\ \varepsilon_{CO_2} = 3.8,\ \varepsilon_{Ar} = 0.0,\ \varepsilon_{He} = 0.0$				
	$H + O_2 (+Ar) = HO_2 (+Ar)$[b]	4.65E+12	0.44	0.00	[24]
	Low-pressure limit	6.81E+18	−1.20	0.0	[26]
	$H + O_2 (+He) = HO_2 (+He)$[c]	4.65E+12	0.44	0.00	[24]
	Low-pressure limit	9.19E+18	−1.20	0.0	[24] × 1.5
10	$H_2 + O_2 = H + HO_2$	5.176E+05	2.43	5.350E+04	[55] × 0.70
11	$HO_2 + H = OH + OH$	7.079E+13	0.00	2.950E+02	[57]
12	$HO_2 + O = OH + O_2$	3.250E+13	0.00	0.0	[52]
13	$HO_2 + OH = H_2O + O_2$	2.456E+13	0.00	−4.970E+02	[51] × 0.85
14	$HO_2 + HO_2 = H_2O_2 + O_2$	1.300E+11	0.00	−1.630E+03	[54]
	$HO_2 + HO_2 = H_2O_2 + O_2$	3.658E+14	0.00	1.200E+04	[54] × 0.87
15	$H_2O_2 (+M) = OH + OH (+M)$[d]	2.000E+12	0.90	4.875E+04	[41]
	Low-pressure limit	2.490E+24	−2.30	4.875E+04	[41]
	$\varepsilon_{H_2} = 3.7,\ \varepsilon_{CO} = 2.8,\ \varepsilon_{CO_2} = 1.6,\ \varepsilon_{N_2} = 1.5,\ \varepsilon_{O_2} = 1.2$				
	$\varepsilon_{He} = 0.65,\ \varepsilon_{H_2O_2} = 7.7,\ \varepsilon_{H_2O} = 0.0$				
	$H_2O_2 (+H_2O) = OH + OH (+H_2O)$[e]	2.000E+12	0.90	4.875E+04	[41]
	Low-pressure limit	1.865E+25	−2.30	4.875E+04	[41]
16	$H_2O_2 + H = H_2O + OH$	2.410E+13	0.00	3.970E+03	[36]
17	$H_2O_2 + H = H_2 + HO_2$	2.150E+10	1.00	6.000E+03	[37]
18	$H_2O_2 + O = OH + HO_2$	9.550E+06	2.00	3.970E+03	[36]
19	$H_2O_2 + OH = H_2O + HO_2$	1.740E+12	0.00	3.180E+02	[40]
	$H_2O_2 + OH = H_2O + HO_2$	7.590E+13	0.00	7.269E+03	[40]
20	$CO + O (+M) = CO_2 (+M)$	1.362E+10	0.00	2.384E+03	[59] × 0.75
	Low-pressure limit	1.173E+24	−2.79	4.191E+03	[58] × 0.87
	$\varepsilon_{H_2} = 2.0,\ \varepsilon_{H_2O} = 12,\ \varepsilon_{CO} = 1.75,\ \varepsilon_{CO_2} = 3.6,\ \varepsilon_{He} = 0.7,\ \varepsilon_{Ar} = 0.7$				
21	$CO + O_2 = CO_2 + O$	1.119E+12	0.00	4.770E+04	[36]
22	$CO + OH = CO_2 + H$	7.015E+04	2.05	−3.557E+02	[63]
	$CO + OH = CO_2 + H$	5.757E+12	−0.66	3.318E+02	[63]
23	$CO + HO_2 = CO_2 + OH$	1.570E+05	2.18	1.794E+04	[64]
24	$HCO + M = H + CO + M$	4.750E+11	0.66	1.487E+04	[10]
	$\varepsilon_{H_2} = 2.0,\ \varepsilon_{H_2O} = 12,\ \varepsilon_{CO} = 1.5,\ \varepsilon_{CO_2} = 2.0$				
25	$HCO + O_2 = CO + HO_2$	7.580E+12	0.00	4.100E+02	[92]
26	$HCO + H = CO + H_2$	7.340E+13	0.00	0.0	[93]
27	$HCO + O = CO + OH$	3.020E+13	0.00	0.0	[36]
28	$HCO + O = CO_2 + H$	3.000E+13	0.00	0.0	[36]
29	$HCO + OH = CO + H_2O$	1.020E+14	0.00	0.0	[52]
30	$HCO + HO_2 = CO_2 + H + OH$	3.000E+13	0.00	0.0	[36]
31	$HCO + HCO = H_2 + CO + CO$	3.000E+12	0.00	0.0	[36]

[a] $F_{cent} = 0.67$.
[b] $F_{cent} = 0.70$.
[c] $F_{cent} = 0.59$.
[d] $F_{cent} = 0.43$.
[e] $F_{cent} = 0.51$.

Table 2
OH^* Chemiluminescence reaction mechanism (units: cm^3/mol/s/cal).

#	Reaction	A	n	E_A	Ref.
32	$H + O + M = OH^* + M$	1.500E+13	0.00	5.975E+03	[71]
	$\varepsilon_{H_2O} = 6.5,\ \varepsilon_{O_2} = 0.4,\ \varepsilon_{N_2} = 0.4,\ \varepsilon_{Ar} = 0.35$				
33	$OH^* + O_2 = OH + O_2$	2.100E+12	0.50	−4.820E+02	[72]
34	$OH^* + H_2 = OH + H_2$	2.950E+12	0.50	−4.440E+02	[72]
35	$OH^* + N_2 = OH + N_2$	1.080E+11	0.50	−1.242E+03	[72]
36	$OH^* + Ar = OH + Ar$	1.690E+12	0.00	4.135E+03	[94]
37	$OH^* + H_2O = OH + H_2O$	5.930E+12	0.50	−8.610E+02	[72]
38	$OH^* + CO_2 = OH + CO_2$	2.750E+12	0.50	−9.680E+02	[72]
39	$OH^* + CO = OH + CO$	3.230E+12	0.50	−7.870E+02	[72]
40	$OH^* + OH = OH + OH$	6.010E+12	0.50	−7.640E+02	[72]
41	$OH^* = OH + hv$	1.450E+06	0.00	0.0	[95]

3.2.3.1. $\dot{H} + O_2$ (+M) $\leftrightarrow H\dot{O}_2$ (+M) *(R9).* This chain propagation reaction, which competes with R1, controls the low-temperature reactivity and requires a pressure-dependent rate constant expression. A new pressure- and temperature-dependent rate constant for this key reaction has been determined by Fernandes et al. [24] over a pressure range of 1.5–950 bar and in the temperature range 300–900 K. This rate constant is based on experimental measurements in a high-pressure flow cell. The pressure and temperature range of R9 was further extended, using unimolecular rate theory. However, the low-pressure limit rate constant proposed by Fernandes et al. [24] for argon as a bath gas reduces the reactivity of the mixture and results in excessively long shock tube ignition delays in the temperature range 1000–1200 K. Bates et al. [26] studied this reaction experimentally in argon over a temperature range of 1020–1260 K and over a pressure range of 10–150 bar, whereas Fernandes et al. performed argon experiments in a lower temperature range of 300–900 K. Combining the low-pressure limit rate constant from Bates et al. with the high-pressure limit from Fernandes et al. results in the best agreement of our mechanism with both RCM and shock tube measurements (Fig. 5b). A comparison between the resulting "hybrid" expression and the experimental measurement on which the fits were based is presented in the Supplementary Material and shows very good agreement (Fig. S4).

Recent flame speed measurements in helium as a bath gas from Burke et al. [16] show a strong pressure dependence of the mass burning rate. The low-pressure limit defined by Fernandes et al. [24] for a temperature range of 300–900 K results in an overprediction of the burning rate at ($T \geqslant 1500$ K) and does not accurately reproduce the negative dependence with increasing pressure. Michael et al. [39] studied this reaction in various bath gases near the low-pressure limit. Their work suggests that experiments performed in Ar have slightly higher rate constants than in He. However, interestingly, mechanisms recently published by Burke et al. [16] and Hong et al. [6] use, respectively, an efficiency and a low-pressure limit that are higher for He than Ar. In the present study, increasing the low-pressure limit by a factor of 1.5 results in better agreement of mass burning rates.

3.2.3.2. HO_2 (+M) $\leftrightarrow \dot{O}H + \dot{O}H$ (+M) *(R15).* The second main pressure-dependent reaction involves the dissociation of hydrogen peroxide into two hydroxyl radicals. Under high-pressure and low- to intermediate-temperature conditions, ignition delay times are highly sensitive to this chain-branching reaction R15 (Fig. 2). Pressure-dependent rate constant expressions for this reaction have recently been published by Hong et al. [40] and by Troe [41]. Hong et al. [40] performed a shock tube study at 1.8 atm over a temperature range of 1020–1460 K and suggested a new low-pressure limit rate constant together with a high-pressure limit rate constant from Sellevåg et al. [6,42]. Troe [41] reviewed the experimental data, performed a theoretical study, and derived a pressure-dependent rate constant expression. The Hong et al. and Troe rate constant expressions have been implemented separately in our current reaction mechanism and tested against the ignition delay times measured by Mittal et al. (Fig. 5c). Both expressions use a higher high-pressure limit than that employed in the Ó Conaire mechanism. Thus, the resulting rate constants present steeper fall-off behavior (see Fig. S5 in the Supplementary Material), and their rate constants are lower at low pressure and higher at high pressure. This results in increased pressure dependence of the system. Using the Hong et al. rate constant expressions [40] results in the prediction of accurate ignition delay times at 15 bar but predicts too high a reactivity at both 30 and 50 bar (Fig. 5c). Troe's study [41] covers a wider pressure and temperature range, and the use of his recommended set of rates accurately predicts the pressure dependence of the system. In this case, ignition delay times are accurately predicted for all three pressures. Troe's set of rate constants has been adopted for R15 in association with the set of rate constants for R9 from Fernandes [24] and Bates [26] previously discussed in Section 3.2.3 (Fig. 5c).

3.2.4. $H_2O_2 + \dot{O}H \leftrightarrow H_2O + H\dot{O}_2$ *(R19)*

This reaction requires the sum of two rate constant expressions to accurately reproduce its temperature dependence. The sum of two rate expressions for $H_2O_2 + \dot{O}H = H_2O + H\dot{O}_2$ published by Hong et al. [40] has been compared with the two previously recommended by Hippler and Troe [43]. These rate constant expressions have been tested by combination with and without the rate constant proposed for H_2O_2 decomposition by Hong et al. and by Troe. We observe a low sensitivity of the mechanism to these reactions for the conditions depicted in Figs. 2 and S2, and have adopted the recent sum of two rate constant expressions from Hong et al. [40].

3.2.5. $\dot{H} + \dot{O}H + M \leftrightarrow H_2O + M$ *(R8)*

Flame speed calculations are very sensitive to this recombination reaction forming water. Increasing this reaction rate decreases reactivity. In our previous mechanism, we used the value reported by Tsang and Hampson [36], but multiplied it by a factor of 2. More recently, Srinivasan and Michael [44] performed a shock tube study of the thermal decomposition of water at high temperature (2196–2792 K) and low pressure (6 and 11 Torr) using Kr as the bath gas. They defined a new rate constant with an evaluated accuracy of ±18%. However, this resulting rate constant is a factor of 2 lower than the rate constant we previously used, resulting in overestimation of flame speeds. Some scattering still exists for this reaction rate, and Konnov [5] estimated the remaining uncertainty of this reaction rate to be a factor of 2. Li et al. [7] also modified the rate constant recommended by Tsang and Hampson [36]. More recently, Sellevåg et al. [45] studied this reaction and recommended a new rate constant, lower than previous recommendations. We have optimized our mechanism, recommending a rate constant that is slightly lower than Li's recommendation, and adopted the efficiencies recommended in the GRI mechanism [12] to get the best agreement of our mechanism with flame speed data (see Fig. S6 in the Supplementary Material).

3.2.6. Other reactions

3.2.6.1. $H_2 + \dot{O}H \leftrightarrow \dot{H} + H_2O$ *(R3).* Similar to reaction R8 above, flame speed predictions are also very sensitive to this reaction under fuel-lean conditions. The rate constant from Michael and Sutherland [46] previously used has been replaced by the very recent rate constant recommended by Lam et al. [47]. The rate constant was measured using UV laser absorption of ȮH radicals behind reflected shock waves over a temperature range of 902–1518 K and a pressure range of 1.15–1.52 atm. They observed a very small experimental scatter (less than 7%), which results in a reduced uncertainty of ±17%. Their recommendation is consistent with the previous work from Michael and Sutherland [46] and Oldenborg et al. [48].

3.2.6.2. $H\dot{O}_2 + \dot{O}H \leftrightarrow H_2O + O_2$ *(R13).* This chain termination reaction, which is highly sensitive for fuel-lean flames (Fig. 3), has been studied experimentally and theoretically by many authors [9,49–53]. However, there is a large discrepancy in the reported rate constant at intermediate temperatures; it can be up to a factor of 4 at 1200 K, due to an unusual temperature dependence of the rate constant, which creates an important non-Arrhenius behavior. The reported rate constant measurements show a deep and narrow minimum around 1250 K. This behavior led to some authors having up to five expressions in order to reproduce the temperature dependence. This reaction has very recently been investigated

experimentally by Hong et al. [49]. Their results are in good agreement with an earlier study by Srinivasan et al. [50], and the authors concluded that there is only a weak temperature dependence and recommended the rate constant reported by Baulch et al. [52], who recommended the rate constant defined by Keyser et al. [51] (see Fig. S7 in the Supplementary Material). However, they recommended that future work be carried out to measure this reaction rate in the intermediate temperature range (900–1200 K), due to a lack of data. Finally, Burke et al. [9] recently reported theoretical work from Harding and Klippenstein [53], which also suggests weak temperature dependence. We adopted the rate constant defined by Keyser et al. [51] but have reduced it by 15% to improve model agreement.

3.2.6.3. $H\dot{O}_2 + H\dot{O}_2 \leftrightarrow H_2O_2 + O_2$ *(R14).* This reaction inhibits reactivity under low-temperature, high-pressure conditions. This is due to the competition with reaction R17. If $H\dot{O}_2$ reacts will H_2, it produces one H_2O_2, which will decompose into two $\dot{O}H$ radicals. Thus, one $H\dot{O}_2$ radical leads to the production of two $\dot{O}H$ radicals. In contrast, reaction R14 consumes two $H\dot{O}_2$ radicals and produces one H_2O_2, thus leading to two $\dot{O}H$ radicals, whereas four $\dot{O}H$ radicals could have been formed through the other pathway. Therefore, this reaction can be considered inhibitive under these conditions. It requires the sum of two rate constants to accurately reproduce its temperature dependence. The previously used set of rate constants from Hippler et al. [54] has been slightly reduced (by 13%).

3.2.6.4. $H_2 + O_2 \leftrightarrow H\dot{O}_2 + \dot{H}$ *(R10).* The rate constant used in the mechanism from Conaire et al. was taken from Tsang and Hampson [36] and is a two-parameter Arrhenius fit. However, the use of this rate constant increased the initial reactivity in flow reactor simulations of the Mueller et al. [28] data and resulted in inaccurate predictions. Therefore, the more recent rate constant defined by Michael et al. [55] was chosen due to its more accurate non-Arrhenius three-parameter fit and its pre-exponential factor has been reduced by 30% in order to reduce the reactivity at low temperature and keep the same reactivity at high temperature.

3.3. CO submechanism

The CO mechanism initially comes from one prepared by Ó Conaire [56], which is based on the mechanism from Mueller et al. [57] and has been updated with recently published rate constants. Based on the sensitivity analysis performed (Fig. 4), only four reactions involving CO appear to be important in this system dominated by hydrogen chemistry:

$$CO + \ddot{O}(+M) \leftrightarrow CO_2(+M) \quad (R20)$$

$$CO + O_2 \leftrightarrow CO_2 + \ddot{O} \quad (R21)$$

$$CO + \dot{O}H \leftrightarrow CO_2 + \dot{H} \quad (R22)$$

$$CO + H\dot{O}_2 \leftrightarrow CO_2 + \dot{O}H. \quad (R23)$$

These four reactions are discussed below. Moreover, syngas oxidation does not show great sensitivity to the HCO submechanism. However, these reactions are important for flame speed predictions of larger hydrocarbons (as shown by Li et al. [10] in Figs. 12, 21, 26 of their work).

3.3.1. $CO + \ddot{O} + M \leftrightarrow CO_2 + M$ *(R20)*

Initially, this reaction was described with a Lindemann fall-off expression, adopting the low-pressure limit from Westmoreland et al. [58] and the high-pressure limit from Troe [59]. However, this combination does not accurately reproduce the pressure dependence of rich, high-CO-content syngas flames, such as those measured by Sun et al. [60], resulting in an over-estimation of the flame speed. Sun et al. [60] recommended the rate constant defined by Baldwin et al. [61], which increases the inhibiting effect of CO. However, adopting this rate constant results in overestimation of the ignition delay times measured at 70 bar in the rapid compression machine (Fig. 9) for high CO concentrations, not accurately capturing the inhibiting effect of CO addition. Moreover, the CO inhibiting impact on ignition delay times measured by Mittal et al. [13] is not well reproduced at either 15 or 30 bar. New flame speed measurements (Fig. 10) highlight the uncertainty, especially for rich mixtures, and suggest that further work may be needed at high pressure and at high CO concentrations. The satisfactory agreement was obtained by adopting the Lindemann fall-off expression and third body efficiencies recommended by Davis et al. [8] but reduced by 13% and 25% for the low- and high-pressure limits, respectively.

3.3.2. $CO + \dot{O}H \leftrightarrow CO_2 + H$ *(R22)*

The rate constant used in our mechanism for the reaction between CO and $\dot{O}H$ was initially taken from Li et al. [10]. As stated by Li et al., based on the work of Zhao et al. [62], the laminar flame

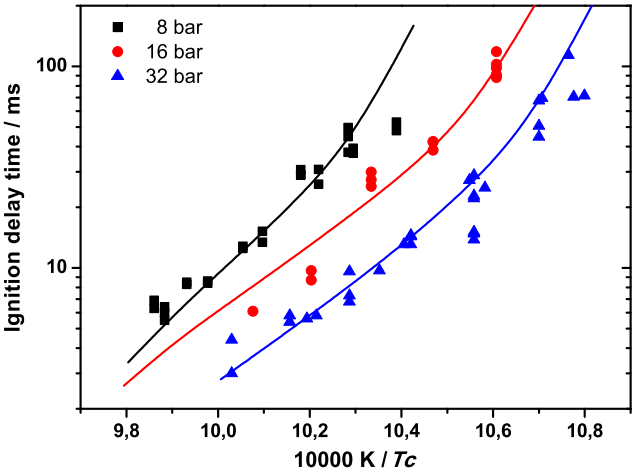

Fig. 6. Effect of pressure on ignition delay times of hydrogen measured in a RCM in NUI Galway (17.36% H_2 + 17.36% O_2 + 32.64% N_2 + 32.64% Ar).

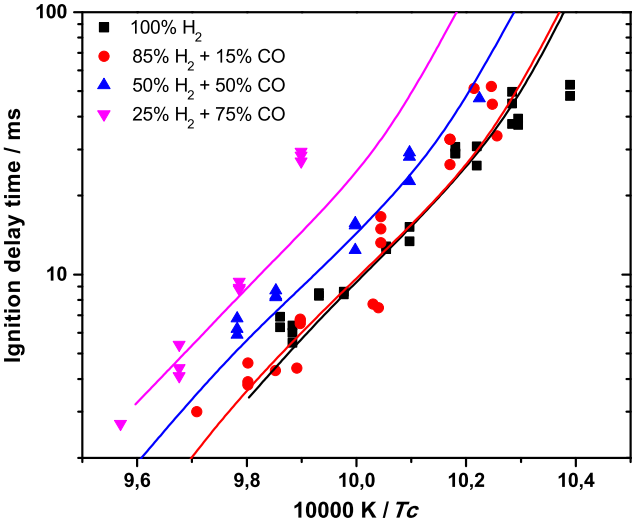

Fig. 7. Effect of CO concentration on ignition delay times of syngas mixtures measured in a RCM in NUI Galway (*Pc* = 8 bar—17.36%(αH_2 + (1− α)CO) + 17.36% O_2 + 32.64% N_2 + 32.64% Ar).

speed prediction is highly sensitive to the reactions $CO + \dot{O}H = CO_2 + \dot{H}$ and $H\dot{C}O + M = \dot{H} + CO + M$. To obtain better agreement with flame speed measurements for syngas mixtures, the Zhao et al. single reaction rate constant for the former reaction was replaced by the set of two reactions proposed as a result of the theoretical study performed by Joshi and Wang [63].

3.3.3. $CO + H\dot{O}_2 \leftrightarrow CO_2 + \dot{O}H$(R23)

This reaction is the most sensitive of the CO subsystems under the conditions investigated (Fig. 4). The rate constant used for this reaction was updated taking the rate constant recently published by You et al. [64]. According to many authors [65–67], this rate constant considerably improves the prediction of RCM results published by Mittal et al. [13].

3.4. $\dot{O}H^*$ submechanism

Most of the ignition delay times recorded in shock tubes are based on the measurement of the chemiluminescence of $\dot{O}H^*$, either at the onset of the emission [68], the maximum rate of increase of the emission [69], or the peak of the $\dot{O}H^*$ emission [70]. Therefore, it is important to predict an accurate $\dot{O}H^*$ emission profile. Kathrotia et al. [71] recently published a new sub-mechanism for $\dot{O}H^*$ chemiluminescence based on a previous study by Tamura [72] and updated with a new rate constant for the formation of $\dot{O}H^*$ via $\dot{O} + \dot{H} + M \leftrightarrow \dot{O}H^* + M$ measured during shock tube experiments. The rate constant of this reaction has no effect on the timing of the $\dot{O}H^*$ profile and hence the ignition delay times derived. Therefore, the results herein are not dependent on the rate constant of this $\dot{O}H^*$ reaction (and hence the absolute value of OH^* concentration). This submechanism has been added to the H_2/CO mechanism to predict accurately the ignition delay times measured in shock tubes.

4. Experimental facilities

4.1. Rapid compression machine

4.1.1. NUIG Combustion Chemistry Centre

Experiments were conducted in the RCM facility at NUI Galway. The RCM is a horizontally opposed twin-piston device, which has been described previously [73,74]. The symmetry of the device helps to reduce the aerodynamic effects inside the combustion chamber at the end of the compression process [75]. The piston heads have been designed to include a uniquely shaped crevice that captures the piston corner vortex, thereby maximizing the homogeneity of the temperature field at full compression. As a result, the aerodynamic effect is reduced in the combustion chamber and both the temperature field and the mixture composition are homogeneous at the end of the compression process.

The thermodynamic conditions reached after the adiabatic compression process are relevant to gas turbine conditions. Top dead center (TDC) is reached after 16–17 ms and the pistons are held in place to ensure constant-volume conditions. In this study, different end-of-compression conditions are achieved by adjusting the initial pressure and temperature. Fuel–oxidizer mixtures were prepared manometrically in stainless steel tanks using gases with a purity of 99.9% or higher. The gases were mixed with an electronic stirrer in the tank. The experimental conditions are presented in Table 3.

For each experiment, the pressure was measured with a pressure transducer (Kistler 603B). The positions of both pistons were measured with a shaft encoder. Both measurements were recorded using a digital oscilloscope. From the pressure profile, the compression time and the ignition delay time were both extracted.

Table 3
Mixture composition for the ignition delay times experiments in the RCM from NUI Galway.

H_2 (%)	CO (%)	O_2 (%)	N_2 (%)	Ar (%)	T_c (K)
17.36	0.00	17.36	32.64	32.64	929–1014
14.76	2.60	17.36	32.64	32.64	940–1032
8.68	8.68	17.36	32.64	32.64	932–1022
4.34	13.02	17.36	32.64	32.64	963–1049

These data are new for this paper .

The ignition delay time was defined as the time interval between the end of the compression process and the maximum rate of increase of the pressure.

For each experiment with a reactive mixture, an experiment with the corresponding nonreactive mixture was performed by replacing the oxygen with nitrogen in the test mixture. Because nitrogen and oxygen have similar thermodynamic properties, the recorded pressure profile presents the same pressure drop as the reactive profile as a result of very similar heat loss properties. The reason for recording a pressure profile for each experiment with a nonreacting mixture was to characterize real heat losses in the kinetic simulations by producing a volume profile, assuming adiabatic compression and expansion processes and frozen chemistry, and using this as input in Chemkin's Aurora [20].

The experimental end-of-compression temperature, T_c, was calculated using the initial temperature, T_i, and pressure, p_i, and the end-of-compression pressure, p_c. Calculations assumed adiabatic compression and frozen chemistry. They were carried out using Gaseq [76], which considers the temperature and the mixture composition dependence of the heat capacity in

$$ln\left(\frac{p_c}{p_i}\right) = \int_{T_i}^{T_c} \frac{\gamma}{\gamma - 1}\frac{dT}{T} \tag{2}$$

4.1.2. UCONN RCM facility

The experimental setup consists of a newly built rapid compression machine, a flow control/supply system, and a mixing chamber. Both the rapid compression machine and the mixing chamber along with the manifolds have a provision for heating up to a maximum temperature of 420 K. For the current study, in order to cover the target range of water addition, the whole experimental setup is heated to a temperature of 400 K.

The new RCM is similar to the one built by Mittal [77], with capability enhancements for attaining higher compression pressures and a wider range of compression ratios. The general details of the predecessor can be found from [78], while the details of the new RCM setup can be found in [79]. The new RCM was tested for consistency with the old RCM result for H_2/O_2 mixtures at various preheat temperatures [79]. The mixture compositions are presented in Table 4.

The RCM consists of a reaction chamber in which the reactant gases are compressed by a creviced piston arrangement. The creviced piston, as shown by Mittal and Sung [78], improves the temperature uniformity substantially. An arrangement of a high-pressure air tank and a pneumatic cylinder drives the creviced

Table 4
Mixture composition for the ignition delay times experiments in the RCM from the University of Connecticut.

H_2 (%)	CO (%)	O_2 (%)	N_2 (%)	T_c (K)
12.500	0.000	6.250	81.250	914–1010
6.250	6.250	6.250	81.250	929–1031
3.125	9.375	6.250	81.250	959–1052
1.250	11.250	6.250	81.250	973–1068

These data are new for this paper.

piston. The creviced piston is held in place by an arrangement of the pressurized hydraulic cylinder. A 5V square pulse generated from Labview starts the data acquisition and triggers the solenoid to release the pressure of the hydraulic chamber. This results in forward movement of the piston arrangement by the pneumatic system. Toward the end of the compression stroke, the piston is smoothly decelerated and finally stopped by the piston-stopping groove. For the cases presented here, the compression time is less than 30 ms.

The end of the reaction chamber is equipped with a pressure transducer for dynamic measurements and a thermocouple for initial temperature monitoring. The compression ratio of the RCM can be changed by changing the clearance and/or the stroke length. Split shims are used between the hydraulic cylinder and the reaction chamber to vary the clearance, whereas the stroke can be adjusted by using spacers.

The mixing chamber consists of an airtight stainless steel tank, including a magnetic stirrer to aid uniform mixing of the constituents. The tank is provided with a rupture disc as a safety measure against accidental overpressure within the mixing tank. Gases are filled into the mixing chamber by the method of partial pressures to prepare the premixtures before heating them to the desired temperature.

High-purity H_2 (99.999%), CO (99.998%), N_2 (99.999 %), and O_2 (99.993 %) gases are used for this study. It is to be noted that the effect of $Fe(CO)_5$, generally present as an impurity in CO, on combustion can be quite substantial [65,80]. The concentration of $Fe(CO)_5$ can also increase due to prolonged storage in steel tanks [81,82]. To ascertain the initial presence of $Fe(CO)_5$, a test certificate for the gas cylinder was obtained, which showed no presence of $Fe(CO)_5$. In order to avoid the buildup of $Fe(CO)_5$ with time due to storage, the high-purity CO used in this study was obtained in an aluminum tank.

For a given mixture composition, the gas temperature at the end of compression, T_c, is varied by altering the compression ratio, whereas the desired pressure at the end of compression, p_c, is obtained by varying the initial pressure of the reactive mixture.

4.2. Shock tube measurements

4.2.1. TAMU shock tube facility

A stainless steel single-diaphragm shock tube was used to measure ignition delay times (τ_{ign}) behind reflected shock waves (RSW) for H_2/O_2 mixtures diluted in 98% Ar. The driven section is 15.24 cm i.d., 4.72 m long, and the driver section is 7.62 cm i.d., 2.46 m long. Shock wave speeds were measured using five PCB-P113A piezoelectric pressure transducers mounted flush with the inner surface. Post-reflected-shock conditions were determined using the measured incident wave speed extrapolated to the end wall in conjunction with the one-dimensional shock relations. The test pressure was monitored using one PCB-134A located at the end wall and one Kistler 603-B1 located at the side wall, in the same plane as the sapphire window used for the optical diagnostic.

Prior to each experiment, the shock tube was cleaned and the driven section was evacuated to 2×10^{-5} Torr or better using a roughing pump and a turbomolecular pump, in order to avoid any contamination. Mixtures were prepared manometrically in a stainless steel mixing tank, all gases having purity of 99.999% or higher (the purity of CO was 99.9%). More details concerning the description of the shock tube and the experimental procedure are available in [83]. The conditions investigated during this study for the $H_2/O_2/Ar$ mixtures are summarized in Table 5 (ignition delay time measurements along with corresponding conditions behind the RSW are provided as Supplemental Material) and conditions investigated for the $H_2/CO/O_2/Ar$ mixtures are available in Krejci et al. [83].

Table 5
Experimental conditions for the shock-tube study of various H_2/O_2 mixtures diluted in 98% Ar at TAMU.

ϕ	H_2 (mol. %)	O_2 (mol. %)	T_5 (K)	p_5 (atm)
0.3	0.75	1.25	975–1530	1.67 ± 0.12
			1090–1250	14.4 ± 1.9
			1155–1230	32.8 ± 1.4
0.5	1.0	1.0	960–1625	1.65 ± 0.15
			1085–1245	13.3 ± 1.0
			1160–1270	32.8 ± 1.5
1.0	1.33	0.67	1035–1740	1.66 ± 0.23
			1105–1210	14.0 ± 1.3
			1140–1260	33.8 ± 0.9

These data are new for this paper.

Ignition delay times were measured at the sidewall location using emission spectroscopy from the $A^2\Sigma^+ \rightarrow X^2\Pi$ transition of the excited-state hydroxyl radical ($\dot{O}H^*$) with an interference filter centered at 307 ± 10 nm with a Hamamatsu 1P21 photomultiplier tube. The ignition delay time was defined as the time between the passage of the reflected shock wave and the intersection of lines drawn along the steepest rate of change of $\dot{O}H^*$ de-excitation and a horizontal that defines the zero-concentration level, as documented in [83]. Uncertainties in τ_{ign} have two sources: the uncertainty in the determination of T_5 (proven to be maintained below 10 K with the method used [84]) and the uncertainty associated with the determination of the steepest rate of change from the $\dot{O}H^*$ profile. The temperature determination is the most important one and can lead to a relatively significant uncertainty in τ_{ign} for the high-pressure conditions of this study. This is due to a slight boundary-layer effect, which results in an increase in the pressure signal, never higher than 2%/ms. Also, the time used during this study is reduced to less than 2 ms (typically less than 1.5 ms). Burke et al. [9], based on the study of Pang et al. [85], stated that the influence of dp/dt on the ignition delay time is important for ignition delay times longer than 1–2 ms, results yielding the same value for dp/dt = 2.0 and 6.5% below 2 ms. Overall, the corresponding increase in temperature would be less than 10 K for the longest ignition delay times reported herein and can therefore be considered negligible (under the experimental uncertainty due to the shock wave velocity determination and the ignition delay time determination). Overall, the total uncertainty on τ_{ign} reported in this study is less than 10%.

4.2.2. DLR shock tube facility

The experiments were carried out in a high-pressure shock tube with an internal diameter of 9.82 cm. It is divided by aluminum diaphragms into a driver section 5.18 m and a driven section 11.12 m in length. The driven section can be pumped down to pressures below 10^{-6} mbar by a turbomolecular pump. Gas mixtures were prepared manometrically in a stainless steel storage cylinder, which is evacuated using a separate turbomolecular pump to pressures below 10^{-6} mbar. High-purity H_2 ($\geqslant$99.9999%), CO ($\geqslant$99.997%), N_2 ($\geqslant$99.999%), Ar ($\geqslant$99.9999%), and O_2 ($\geqslant$99.9999%) were used for this study. The shock speed was measured over three 20-cm intervals using four piezoelectric pressure gauges. The temperature and pressure behind the reflected shock wave were computed from the measured incident shock speed and the speed attenuation using a one-dimensional shock model. The estimated uncertainty in reflected shock temperatures is less than ±10 K in the temperature range of our measurements. The ignition was observed by measuring pressure profiles with piezoelectric gauges (PCB 113A24 and Kistler) located 1 cm from the end flange. The PCB gauge was shielded by 1-mm polyimide to reduce heat transfer. Also, the $\dot{O}H^*$ at 308 nm at the same po-

sition was selected by a narrow band pass filter (FWHM = 5 nm) and measured with a photomultiplier. All ignition delay time values shown in this paper were determined by measuring the time difference between the initiation of the system by the reflected shock wave and the occurrence of the $\dot{O}H^*$ maximum, because this allows good comparability to the simulations. The experimental setup allows measurements of ignition delay times for observation times up to 6.5 ms, depending on the temperature. Such long ignition delay times are strongly influenced by the pressure increase due to a gas-dynamics effect. This is considered in the simulations presented in Section 2.3. Other effects such as "mild ignition" occuring not close to the end flange are avoided by the dilution of the reactions with Ar.

4.3. Flame speed measurement: TAMU spherical bomb facility

The experimental facility used in this study is an aerospace-grade aluminum constant-volume cylindrical bomb equipped with 12.7-cm-diameter fused quartz windows at each end, providing optical access. More information about the facility and its construction is detailed in de Vries et al. [86] and Lowry et al. [87]. Mixtures were prepared directly in the vessel using the partial pressure method via 0–1000 Torr and 0–500 psi pressure transducers. All gases used in this study were an ultra-high-purity grade ($\geqslant$99.9% for each primary gas). To reduce hydrodynamic instabilities at pressures above atmospheric, helium was used as the diluent, with an O_2:He ratio of 1:7. Experiments with initial pressure 1 atm were performed with standard air. The mixture was spark-ignited from a separate control room using a constant-current power supply, a 10-μF capacitor, an automotive ignition coil, and a solenoid switch. The spark occurs at the center of the vessel, where two 0.9-mm Alloy X electrodes with sharpened tips are separated by a variable gap.

Flame speed experiments were carried out at an initial temperature of 295.7 ± 2.5 K with initial pressures of $1 \pm 6.6 \times 10^{-5}$ atm (0.05 Torr accuracy), and 5 and 10 ± 0.003 atm (0.05 PSI accuracy). The accuracies of the final mixture pressures are the same for every component of the mixture (0.05 Torr for the experiments at 1 atm and on H_2 and CO for the higher pressures and 0.05 PSI for the other components for the experiments above atmospheric pressure).

Flame propagation is recorded for each experiment using a Z-type schlieren setup similar to that described by Settles [88]. Light from a mercury arc lamp is collimated using an f/8 parabolic mirror with diameter 15.2-cm and directed through the optical windows of the experimental vessel. A second parabolic mirror located on the other side of the vessel focuses the collimated beam into a high-speed camera, Photron FastCam SA1.1. Before the light entered the camera, a circular pinhole aperture was placed at the focal point to intensify the density gradients.

5. Results and discussion

The updated kinetic mechanism has been validated over a wide range of oxidation studies, including ignition delays measured in both shock tubes and RCMs, species concentration profiles measured in a flow reactor and JSRs and laminar flame speeds. These studies cover a wide range of temperatures, 800–2500 K, and pressures, 1–50 bar. The performance of the current mechanism is presented below against a selection of targets covering the full range of conditions. A comprehensive validation is available in the Supplementary Material. Burke et al. [9] recently performed a complete comparison of the available literature hydrogen mechanisms. Therefore, only a comparison of the different H_2/CO mechanisms is provided in the Supplementary Material. Moreover, a comparison between the present mechanism and previously published mechanisms against the new experimental data presented in this paper is available in the Supplementary Material.

The performance of the new mechanism has also been compared with the new ignition delay times measured in RCMs and shock tubes for mixtures from pure hydrogen to 5% H_2 + 95% CO over a temperature range of 900–1740 K and for end-of-compression pressure from 1 to 70 bar. The ignition of syngas mixtures, from pure hydrogen to a high concentration of CO, has been studied in two different RCMs. The study at NUI Galway was performed for a lean mixture over a pressure range of 8–32 bar and the study at the University of Connecticut was performed at a higher pressure of 70 bar.

5.1. NUIG RCM measurements

Ignition delay times were recently measured for various lean (ϕ = 0.5) syngas mixtures in the RCM from the Combustion Chemistry Centre (Figs. 6–8 and S9–S11). Measurements were performed at 8, 16, and 32 bar. The mixtures and experimental conditions are provided in Table 3. Over this temperature range, increasing pressure results in higher reactivity of the mixture and shorter ignition delay times. However, for the highest temperatures, a crossover starts to be observed due to the competition between R1 and R9. Increasing the amount of CO in the fuel mixtures results in longer ignition delay times, showing the inhibiting effect of carbon monoxide on the hydrogen chemistry. The kinetic mechanism has been used to simulate these experimental results. The predicted ignition delay times are in very good agreement with experimental results. Both the inhibiting effect of CO and the unusual pressure dependence are well reproduced.

5.2. UCONN RCM measurements

Ignition delay times for various syngas mixtures were measured in the RCM of the University of Connecticut. The study has been performed under stoichiometric conditions with 100%, 50%, 25%, and 10% H_2 in the H_2/CO fuel mixtures with nitrogen dilution at an end-of-compression pressure of 70 bar and an end-of-compression temperature range of 914–1068 K (Fig. 9). The mixture compositions are defined in Table 4. Results show the inhibiting effect of carbon monoxide on the syngas ignition delay times, which increase with increasing amounts of CO in the syngas

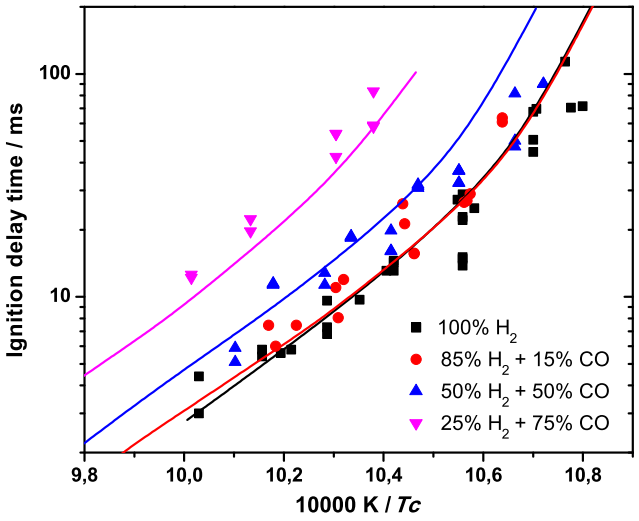

Fig. 8. Effect of CO concentration on ignition delay times of syngas mixtures measured in a RCM in NUI Galway (Pc = 32 bar—17.36%(αH$_2$ +(1 α)CO) +17.36% O_2 +32.64% N_2 +l32.64% Ar).

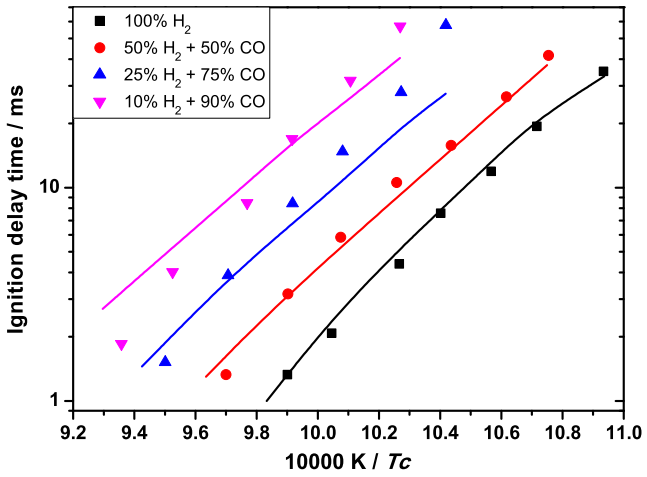

Fig. 9. Effect of CO concentration on ignition delay times measured in a RCM in the University of Connecticut (Pc = 70 bar—12.5%(αH_2 + (1 α)CO) + 6.25% O_2 + 81.25% N_2).

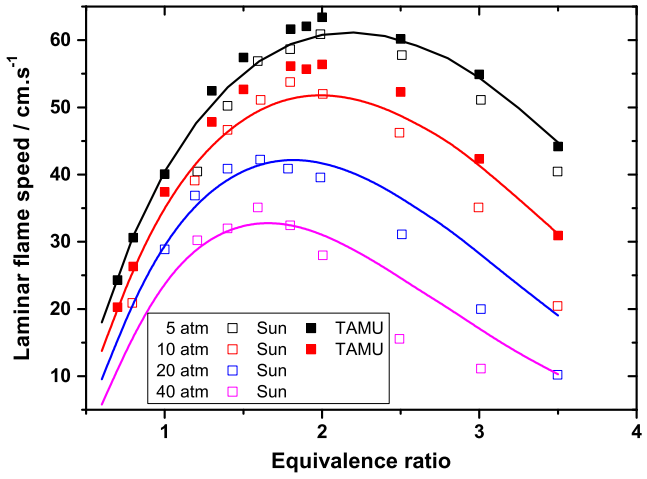

Fig. 10. Comparison with flame speed measurements from Sun et al. [60] and this study (from TAMU) (95% CO + 5% H_2 in O_2 + 7 He—Ti = 298 K)

mixture. However, as noted previously by Mittal et al. [13] and Kalitan et al. [68] at lower pressures, this effect is more significant for fuel mixtures with a CO concentration greater than 50%. The experimental results have been compared to ignition delay time predictions from the present mechanism, Fig. 9. The model captures this inhibiting effect accurately and its predictions are in very good agreement with the experimental results.

5.3. DLR shock tube measurement

Ignition delay times of hydrogen and hydrogen/carbon monoxide mixtures were determined at 1, 4, and 16 bar and at a dilution of 1:5 (dilution 1:5 means one part of a fuel/oxygen/inert gas mixture, defined by the equivalence ratio and a ratio of 21/79 for oxygen/inert gas, and four parts of the inert gas). The mixture compositions are provided in Table 6. In addition to the hydrogen measurements at equivalence ratios of $\phi = 0.5$ and 1.0 [70], the ignition delay times of very lean ($\phi = 0.1$) and fuel-rich mixtures ($\phi = 4.0$) and the influence of nitrogen at $\phi = 0.5$ as an inert gas were determined. Experiments with different ratios of H_2/CO (50%/50%, 5%/95%) were performed to determine the influence of CO on the ignition of syngas. The ignition delay times of two H_2/CO/N_2/Ar mixtures (H_2/CO = 85%/15% and 50%/50%, 50% N_2, and 50% Ar) were also determined at 16 bar.

The results of measurements are shown in Figs. 11–15 (and S12–S14 in the Supplementary Material) together with simulations.

The simulations agree very well with the measurements. The complex pressure and inert gas dependence of the hydrogen and syngas mixtures is very well predicted. Deviations between the experiments and the simulations of hydrogen and syngas ignition can only be observed for the longest ignition delay times. This is probably caused by small deviations of the assumed and the real temperature profiles, which exhibit a very pronounced influence on the ignition delay times. For the 5% H_2/95% CO mixture at $\phi = 0.5$, Fig. 13, the simulations predict longer ignition delay times at high temperatures. This may be caused by problems of determining short ignition delay times due to the very broad $\dot{O}H^*$ maximum, see discussion below.

Figure 16 shows a comparison of the measured ignition delay times of the syngas mixtures at about 4 bar and $\phi = 1.0$ together with values for H_2 at equivalence ratios $\phi = 0.1$ and 1.0 [70]. It can be seen that the characteristics of both of the H_2/CO mixtures and of H_2 are similar. At higher temperatures, a lower activation energy is observed, followed by a very steep increase at about 1000 K. The ignition behavior is dominated by the hydrogen content of the mixtures. The addition of 50% CO has only a small influence on the measured ignition delay times. The syngas mixture with 5% H_2/95% CO shows much longer ignition delay times at higher temperatures than the other hydrogen-containing mixtures and compared to a H_2/O_2/Ar mixture ($\phi = 0.1$) with a similar low hydrogen content. This can be explained by the shape of the pressure and $\dot{O}H^*$ emission profiles, Fig. 17. The pressure profiles show only a slight increase of the signal for a long time and the $\dot{O}H^*$ signal shows a very broad peak beginning with a steep increase, followed by a slower increase to a maximum. These characteristics are well reproduced by the simulations, Fig. 18, which represents simulations for the experiment in Fig. 17 (full lines) and a H_2/O_2/Ar mixture with the same hydrogen content ($\phi = 0.5$, CO replaced by Ar, dashed lines) at 1240 K and 3.79 bar. It can be seen

Table 6
Experimental conditions for the shock-tube experiments at DLR.

Fuel (H_2/CO) (%)	ϕ	H_2 (mol.%)	CO (mol.%)	O_2 (mol.%)	N_2 (mol.%)	Ar (mol.%)	T_5 (K)	p_5 (atm)
100/0	0.1	0.81		4.03		95.16	925–2100	1, 4, 16
	0.5	3.47		3.47	93.06		950–2000	1, 4, 16
	4.0	12.54		1.57		85.89	935–1850	1, 4, 16
85/15	0.5	2.98	0.52	3.51	46.57	46.42	1020–1220	16
50/50	0.5	1.74	1.74	3.47		93.06	870–2100	1, 4, 16
	0.5	1.74	1.74	3.52	47.32	45.68	1000–1220	16
	1.0	2.96	2.96	2.96		91.12	910–2170	1, 4, 16
5/95	0.5	0.17	3.30	3.47		93.06	940–2220	1, 4, 16
	1.0	0.30	5.62	2.96		91.12	950–2200	1, 4, 16

These data are new for this paper.

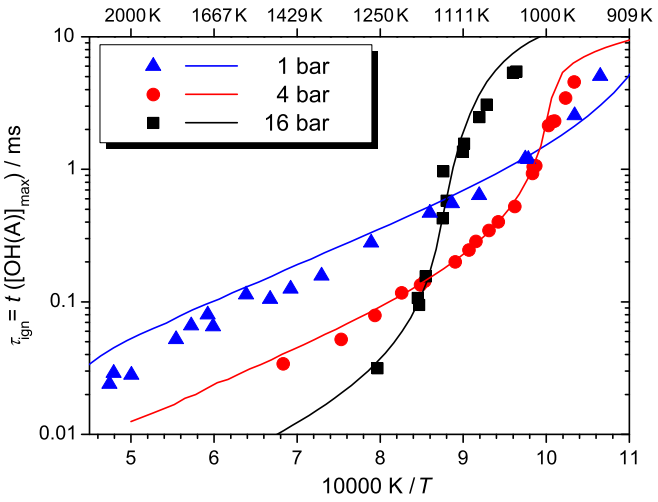

Fig. 11. Measured and calculated ignition delay times of a H_2/O_2/Ar mixture at an equivalence ratio $\phi = 0.1$ and a dilution of 1:5. Experiments were performed in a shock tube at DLR. See Table 6 for mixture composition.

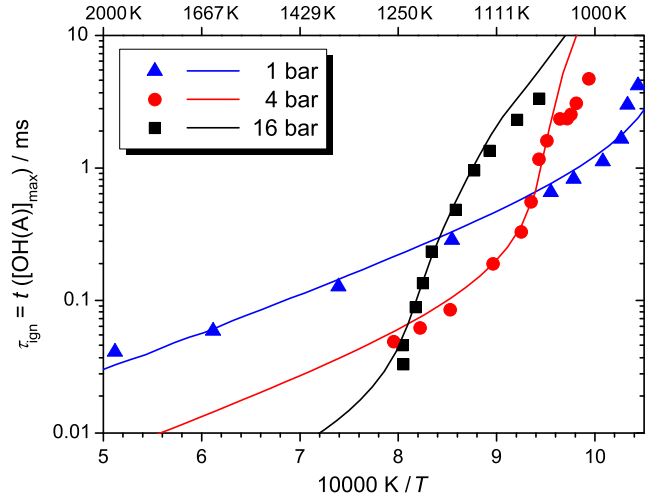

Fig. 12. Measured and calculated ignition delay times of a $H_2/O_2/N_2$ mixture at an equivalence ratio $\phi = 0.5$ and a dilution of 1:5. Experiments were performed in a shock tube at DLR. See Table 6 for mixture composition.

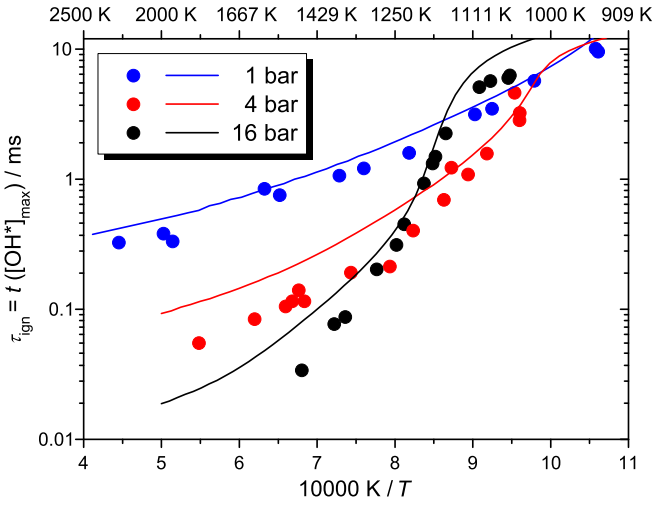

Fig. 13. Measured and calculated ignition delay times of a syngas (5% H_2/95% CO) /O_2/Ar mixture at an equivalence ratio $\phi = 0.5$ and a dilution of 1:5. Experiments were performed in a shock tube at DLR. See Table 6 for mixture composition.

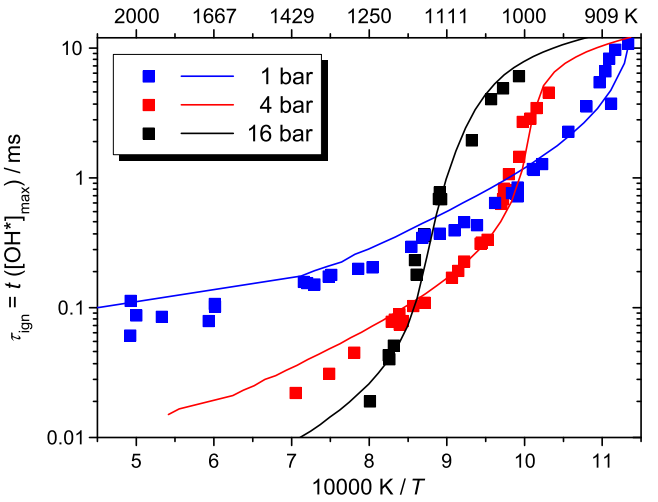

Fig. 14. Measured and calculated ignition delay times of a syngas (50% H_2/50% CO)/ O_2/Ar mixture at an equivalence ratio $\phi = 0.5$ and a dilution of 1:5. Experiments were performed in a shock tube at DLR. See Table 6 for mixture composition.

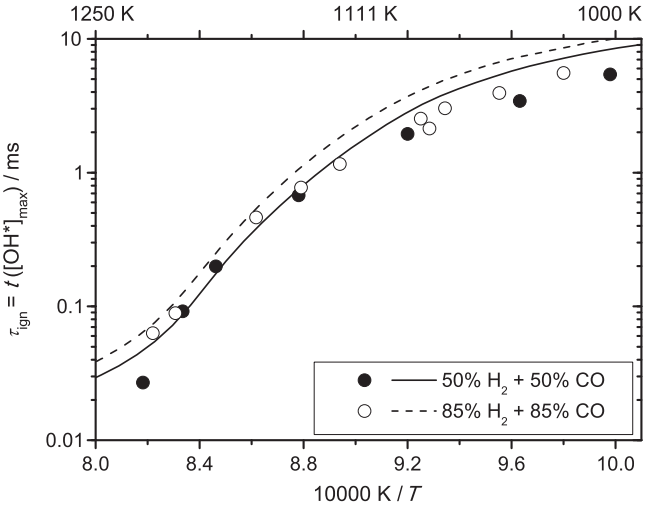

Fig. 15. Measured (symbols) and calculated (lines) ignition delay times of two syngas mixtures (85% H_2/15% CO and 50% H_2/50% CO)/O_2/inert gas (50% Ar/50% N_2) mixture at an equivalence ratio $\phi = 0.5$, a dilution of 1:5 and a pressure $p = 16$ bar. Experiments were performed in a shock-tube at DLR. See Table 6 for mixture composition.

that the hydrogen consumption is fast, causing a steep increase of the $\dot{O}H^*$ signal. The much slower CO consumption is initialized by the hydrogen reactions. The slow CO oxidation causes only a slow temperature increase, so that the observed pressure increase is also slow. The $\dot{O}H^*$ signal is slowly increasing to a maximum due to the production of $\dot{H}$ and $\dot{O}$ atoms by the reactions during the CO oxidation:

$$CO + \dot{O}H \leftrightarrow CO_2 + \dot{H} \quad (R22)$$

$$\dot{H} + O_2 \leftrightarrow \ddot{O} + \dot{O}H \quad (R1)$$

$$\dot{H} + \ddot{O} + (M) \leftrightarrow \dot{O}H^* \quad (R7)$$

Comparing the concentration profiles of the hydrogen and the $CO/H_2/O_2$/Ar mixtures, it can be seen that hydrogen is consumed earlier for the CO/H_2 mixtures due to the reaction $CO + H\dot{O}_2 \leftrightarrow CO_2 + \dot{O}H$ (R23), which transforms a less reactive $H\dot{O}_2$ radical into

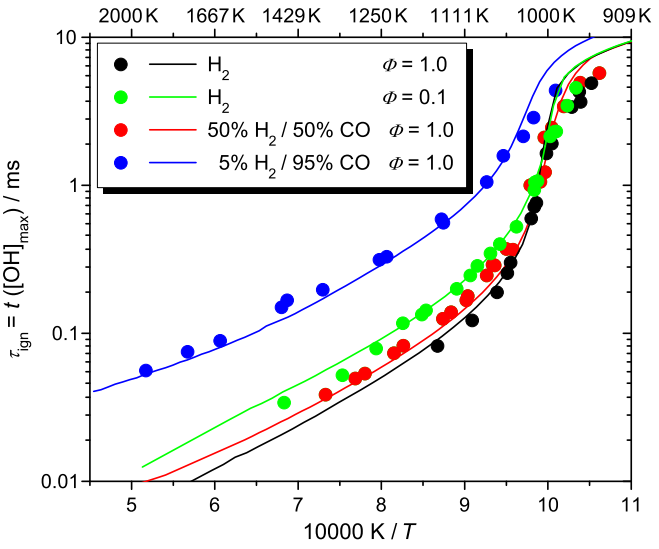

Fig. 16. Measured and calculated ignition delay times of H_2 and syngas/O_2/Ar mixtures at a dilution of 1:5 and a pressure $p = 4$ bar.

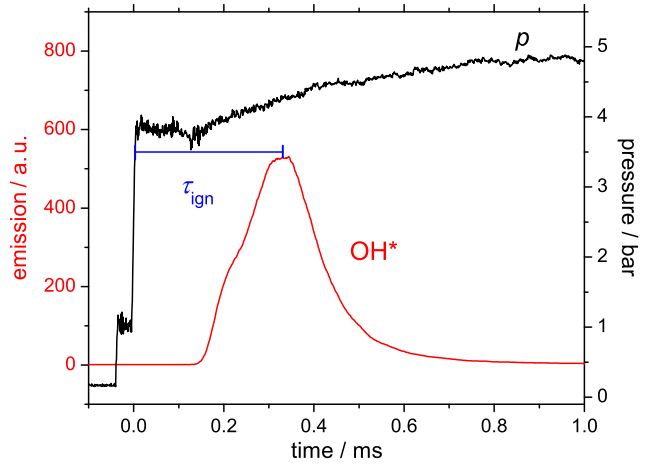

Fig. 17. Pressure and emission signal of a (5% H_2/95% CO)/O_2/Ar mixture ($\phi = 1.0$, dilution 1:5) at $p_5 = 3.79$ bar and $T_5 = 1240$ K.

a more reactive ȮH radical. The faster H_2 consumption leads to an earlier onset of ȮH* production. Nevertheless, the maximum of the ȮH* occurs at significantly longer times for the H_2/CO mixtures than for the pure H_2 mixtures due to the slow oxidation of CO. As we define the ignition delay time as the maximum of the ȮH* signal, significantly longer ignition delay values for the 5% H_2/95% CO mixtures are observed compared to other hydrogen-containing mixtures. Using definitions of the ignition delay times such as "onset of the ȮH* emission" or "maximum heat release rate", ignition delay times of less than 50% of the measured ones would be determined. This problem of the strong dependence of the values of the ignition delay times on their definition is only observed under dilute conditions with high CO content. For the 50% H_2/50% CO mixture (Fig. 19) or for undiluted conditions, the heat release of the hydrogen oxidation and the radical concentrations are much higher, leading to rapid CO oxidation. The consumption of H_2 is also accelerated for undiluted conditions compared to the H_2/O_2/Ar mixture. For the 50% H_2/50% CO mixture, the acceleration of the H_2 ignition is very small. If the 5% H_2/95% CO mixture is further diluted ($\phi = 0.5$, dilution 1:10), the oxidation of CO becomes even slower, causing a very broad ȮH* emission signal with two separated maxima due to the fast oxidation of H_2 and the slow oxidation of CO [89].

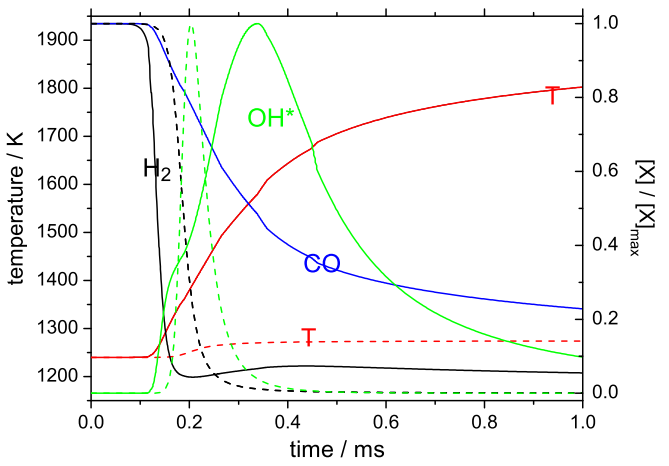

Fig. 18. Calculated temperatures and concentrations of a (5% H_2/95% CO)/O_2/Ar mixture ($\phi = 1.0$, dilution 1:5) and a H_2/O_2/Ar mixture ($\phi = 0.05$, CO of the syngas mixture replaced by Ar) at $p = 3.79$ bar and $T = 1240$ K. Black lines: H_2, green lines: ȮH*, blue line: CO, red lines: temperatures. Full lines: 5% H_2/95% CO, dashed lines: H_2. (For interpretation of the references to color in this figure legend, the reader is referred to the web version of this article.)

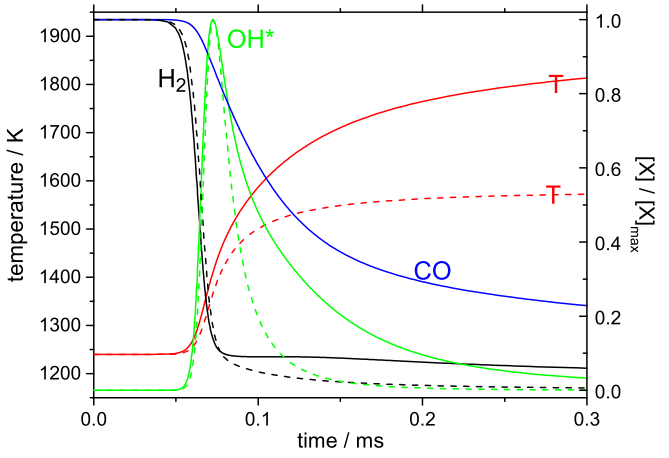

Fig. 19. Calculated temperatures and concentrations of a (50% H_2/50% CO)/O_2/Ar mixture ($\phi = 1.0$, dilution 1:5) and a H_2/O_2/Ar mixture ($\phi = 0.5$, CO of the syngas mixture replaced by Ar) at $p = 3.79$ bar and $T = 1240$ K. Black lines: H_2, green lines: ȮH*, blue line: CO, red lines: temperatures. Full lines: 50% H_2/50% CO, dashed lines: H_2. (For interpretation of the references to color in this figure legend, the reader is referred to the web version of this article.)

5.4. TAMU shock tube measurement

Recently, the ignition of various H_2/CO/O_2 mixtures (with H_2/CO ratios of 80/20, 50/50, 40/60, 20/80, and 10/90) diluted in 98% Ar was studied between 960 and 2000 K. The equivalence ratio was set to 0.5 and pressures ranged from 1.5 to 30 atm [83]. Overall, results showed that an increase in the CO concentration led to an increase in the ignition delay time. This increase in the ignition delay time was, however, more pronounced for mixtures containing more than 50% CO as fuel, and results for the 80% H_2/20% CO mixture would not present any distinguishable difference from the H_2/O_2 results of the present study. For all the mixtures, a crossover in the ignition delay times is observed with increasing temperature. As for the H_2/O_2 mixtures in this study and in [70], it is due to the competition between R1 and R9. This unusual behavior indicates that hydrogen is still governing the reactivity of the H_2/CO mixture (even though an increase in carbon monoxide causes the activation energy of the mixture to decrease slightly in [83]). All

of these results have been successfully reproduced by the model, especially for pressures above 1.6 atm.

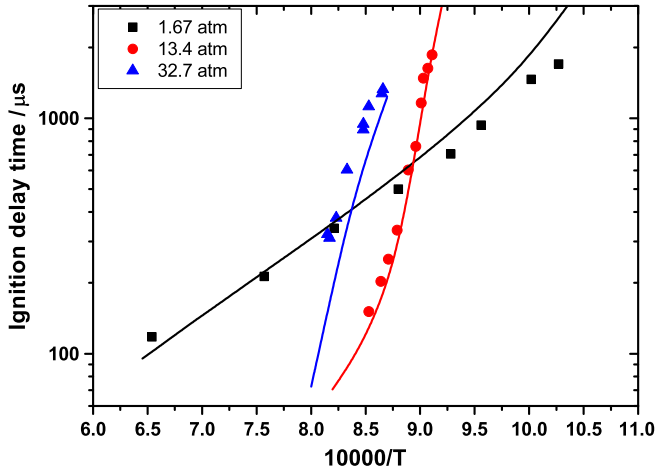

Fig. 20. Ignition delay times of H_2/O_2/Ar mixtures ($\phi = 0.3$) measured in TAMU shock tube.

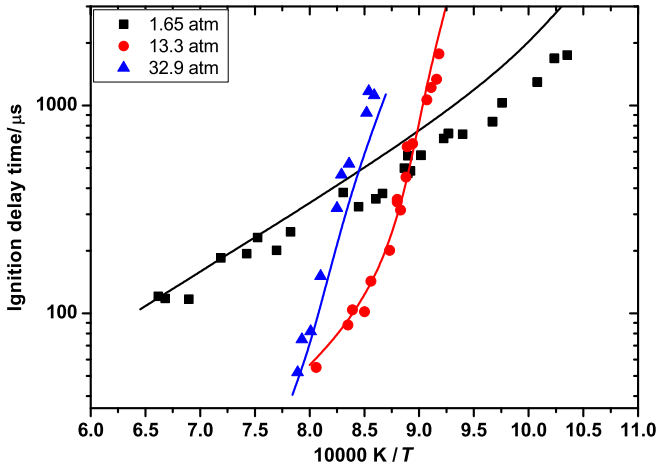

Fig. 21. Ignition delay times of H_2/O_2/Ar mixtures ($\phi = 0.5$) measured in TAMU shock tube.

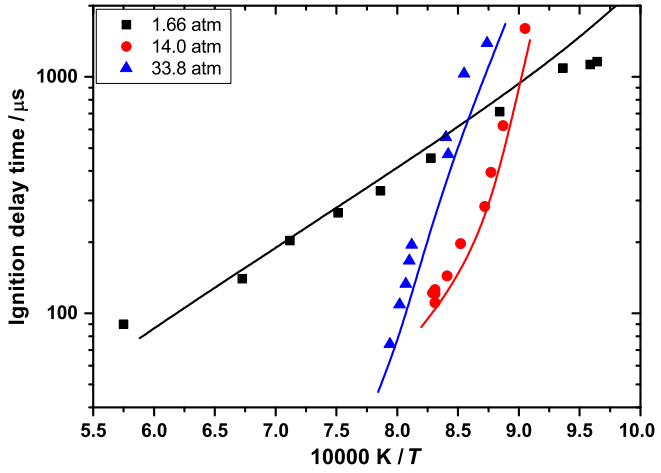

Fig. 22. Ignition delay times of H_2/O_2/Ar mixtures ($\phi = 1.0$) measured in TAMU shock tube.

The ignition delay times of H_2/O_2 mixtures diluted in 98% Ar were determined for three different equivalence ratios: 0.3, 0.5, and 1.0. As can be seen in Fig. S15, for a pressure of around 13 atm, the effect of the equivalence ratio on the ignition delay times is not very significant for H_2/O_2 mixtures under the conditions investigated, and the experimental trends were well captured by the model. A similar result for the effect equivalence ratio was found for the other pressures investigated and in the study of Herzler and Naumann [70]. The pressure dependence on the ignition delay observed for the data from [70] between 1 and 16 bar was also observed with the new data of this study, between 1.6 and 30 atm. As can be seen in Figs. 20–22 for equivalence ratios 0.3, 0.5, and 1.0, respectively, the pressure dependence of hydrogen ignition is well reproduced by the model for all cases and the explanations provided for the results in Fig. 1 also apply to this new set of data obtained at higher pressures.

6. Conclusions

This study presents new oxidation data for hydrogen and syngas mixtures. Flame speed and ignition delay times were measured over wide pressure and temperature ranges of 1–70 bar and 900–2500 K, respectively. Ignition delay times were measured in both RCMs and shock tubes. These new experimental results were compared to an updated mechanism for hydrogen and syngas mixtures with recently published reaction rate constant expressions for several critical reactions. The updated mechanism was validated for different oxidation studies (ignition delay times, flame speed, species profiles) and for a wide range of pressures (1–70 bar), temperatures (900–2500 K), and equivalence ratios (0.1–4.0). The mechanism accurately reproduces high-pressure and intermediate- to high-temperature data relevant to gas turbine conditions and therefore of high interest. Under these particular conditions, the oxidation pathway $H_2 + H\dot{O}_2 \leftrightarrow \dot{H} + H_2O_2$, followed by $H_2O_2\ (+M) \leftrightarrow \dot{O}H + \dot{O}H\ (+M)$, was found to be most crucial for accurate ignition delay time prediction, whereas at low pressure (1 atm) and low temperature (below 1000 K), the reactivity is mainly controlled by the competition between the chain-branching reaction $\dot{H} + O_2 \leftrightarrow \ddot{O} + \dot{O}H$ and the pressure-dependent chain-propagating reaction $\dot{H} + O_2\ (+M) \leftrightarrow H\dot{O}_2\ (+M)$. This reaction was found to inhibit the reactivity of flame speed under very lean conditions and promotes the reactivity under stoichiometric to rich conditions. This behavior is explained by the production of $H\dot{O}_2$ radicals that consume or produce $\dot{O}H$ radicals.

Syngas chemistry is governed by the hydrogen chemistry, and CO addition has an inhibiting effect. This effect is noticeable for CO concentrations of 50% or higher for ignition delay time measurement, but appears for lower CO concentration for flame speed measurements. A CO concentration of 50% in the fuel results in an increase by a factor of 2 in the ignition delay times, whereas a concentration of 90% increases the ignition delay times by a factor of 10. For flame speed, the same concentrations result in a reduction of flame speed by 35% and a factor of 4, respectively. Therefore, the inhibiting effect appears stronger for ignition delay times than for flame speeds, but is only significant for high CO concentrations. New flame speed measurements for syngas mixtures with a high CO concentration at 5 and 10 atm highlighted the remaining uncertainties for rich mixtures. Thus, further work is needed to reduce these uncertainties.

A comparison between the present mechanism and previously published mechanisms is provided in the Supplementary Material. Overall, the predictions of the mechanisms for a series of fundamental shock tube, RCM, and flame speed experiments are in good agreement, and the predictions are also in good agreement with the associated experimental data. However, some differences

appear, especially in the inhibiting effect of CO. The main differences appear at low to intermediate temperature due to the importance of the oxidation pathway through reactions R9, R15, and R17. It is crucial to correctly predict this oxidation pathway in order to correctly reproduce experimental results, and many mechanisms fail. At higher temperature, under shock tube conditions, the reactivity is mainly controlled by reaction R1. The expressions for the rate constant used in the different mechanism are similar, and this results in very good agreement between the predictions and with the experimental data.

Acknowledgments

The NUIG and DLR work is part of the European Project H_2-IGCC funded by the European Commission and funding is gratefully acknowledged. Additional funding provided by Science Foundation Ireland and the Saudi Arabian Oil Company. The LNLL work is performed under the auspices of the U.S. Department of Energy by Lawrence Livermore National Laboratory under Contract DE-AC52-07NA27344. The TAMU work is based upon work supported by the Department of Energy under Award DE-FE0004679. The authors thank C. J. Aul for his help in performing some of the shock-tube experiments, and A. Vissotski, D. Plichta, and S. Ravi for help with the flame speed experiments. A.K. Das and C.J. Sung acknowledge the support for their work at UConn from the Combustion Energy Frontier Research Center, an Energy Frontier Research Center funded by the U.S. Department of Energy, Office of Science, Office of Basic Energy Sciences under Award DE-SC0001198.

Appendix A. Supplementary material

Supplementary data associated with this article can be found, in the online version, at http://dx.doi.org/10.1016/j.combustflame.2013.01.001.

References

[1] C.M. White, R.R. Steeper, A.E. Lutz, Int. J. Hydrogen Energy 31 (10) (2006) 1292–1305.
[2] R. Kuroki, A. Kato, E. Kamiyama, D. Sawada, SAE 2010-01-0581, 2010.
[3] N.J. Killingsworth, V.H. Rapp, D.L. Flowers, S.M. Aceves, J.Y. Chen, R. Dibble, Proc. Combust. Inst. 33 (2010) 3141–3149.
[4] M. Ó Conaire, H.J. Curran, J.M. Simmie, W.J. Pitz, C.K. Westbrook, Int. J. Chem. Kinet. 36 (2004) 603–622.
[5] A.A. Konnov, Combust. Flame 152 (4) (2008) 507–528.
[6] Z. Hong, D.F. Davidson, R.K. Hanson, Combust. Flame 158 (4) (2011) 633–644.
[7] J. Li, Z.W. Zhao, A. Kazakov, F.L. Dryer, Int. J. Chem. Kinet. 36 (10) (2004) 566–575.
[8] S.G. Davis, A.V. Joshi, H. Wang, F. Egolfopoulos, Proc. Combust. Inst. 30 (2005) 1283–1292.
[9] M.P. Burke, M. Chaos, Y. Ju, F.L. Dryer, S.J. Klippenstein, Int. J. Chem. Kinet. 44 (7) (2012) 444–474.
[10] J. Li, Z.W. Zhao, A. Kazakov, M. Chaos, F.L. Dryer, J.J. Scire, Int. J. Chem. Kinet. 39 (3) (2007) 109–136.
[11] H. Wang, X. You, A.V. Joshi, S.G. Davis, A. Laskin, F. Egolfopoulos, C.K. Law, USC Mech. Version II, 2007. <http://ignis.usc.edu/USC_Mech_II.htm>.
[12] G.P. Smith, D.M. Golden, M. Frenklach, N.W. Moriarty, B. Eiteneer, M. Goldenberg, C.T. Bowman, R.K. Hanson, S. Song, J. William C. Gardiner, V.V. Lissianski, Z. Qin, GRI-Mech VERSION 3.0, 1999. <http://www.me.berkeley.edu/gri_mech/>.
[13] G. Mittal, C.J. Sung, R.A. Yetter, Int. J. Chem. Kinet. 38 (8) (2006) 516–529.
[14] D. Lee, S. Hochgreb, Int. J. Chem. Kinet. 30 (6) (1998) 385–406.
[15] D. Bradley, M. Lawes, K. Liu, S. Verhelst, R. Woolley, Combust. Flame 149 (1–2) (2007) 162–172.
[16] M.P. Burke, M. Chaos, F.L. Dryer, Y. Ju, Combust. Flame 157 (4) (2010) 618–631.
[17] S. Gersen, N.B. Anikin, A.V. Mokhov, H.B. Levinsky, Int. J. Hydrogen Energy 33 (7) (2008) 1957–1964.
[18] S.M. Walton, X. He, B.T. Zigler, M.S. Wooldridge, Proc. Combust. Inst. 31 (2007) 3147–3154.
[19] R.J. Kee, F.M. Rupley, J.A. Miller, Chemkin-II: A Fortran Chemical Kinetics Package for the Analysis of Gas-phase Chemical Kinetics, Report No. SAND89-8009, Sandia National Laboratories, 1989.
[20] R.J. Kee, F.M. Rupley, J.A. Miller, M.E. Coltrin, J.F. Grcar, E. Meeks, H.K. Moffat, A.E. Lutz, G. Dixon-Lewis, M.D. Smooke, J. Warnatz, G.H. Evans, R.S. Larson, R.E. Mitchell, L.R. Petzold, W.C. Reynolds, M. Caracotsios, W.E. Stewart, P. Glarborg, C. Wang, C.L. McLellan, O. Adigun, W.G. Houf, C.P. Chou, S.F. Miller, P. Ho, P.D. Young, D.J. Young, D.W. Hodgson, M.V. Petrova, K.V. Puduppakkam, CHEMKIN Release 4.1.1, Reaction Design, San Diego, CA, 2007.
[21] P. Middha, B. Yang, H. Wang, Proc. Combust. Inst. 29 (1) (2002) 1361–1369.
[22] P. Middha, H. Wang, Combust. Theory Modell. 9 (2) (2005) 353–363.
[23] G. Mittal, C.J. Sung, Rapid Compression Machine (RCM) Database, 2009. <http://www.mae.case.edu/facilities/cdl/projects/rapidcomp/rapiddatabase/h2co>.
[24] R.X. Fernandes, K. Luther, J. Troe, V.G. Ushakov, Phys. Chem. Chem. Phys. 10 (29) (2008) 4313–4321.
[25] Z. Hong, D.F. Davidson, E.A. Barbour, R.K. Hanson, Proc. Combust. Inst. 33 (1) (2011) 309–316.
[26] R.W. Bates, D.M. Golden, R.K. Hanson, C.T. Bowman, Phys. Chem. Chem. Phys. 3 (12) (2001) 2337–2342.
[27] C.J. Cobos, H. Hippler, J. Troe, J. Phys. Chem. 89 (2) (1985) 342–349.
[28] M.A. Mueller, R.A. Yetter, F.L. Dryer, Proc. Combust. Inst. 27 (1) (1998) 177–184.
[29] D.A. Masten, R.K. Hanson, C.T. Bowman, J. Phys. Chem. 94 (18) (1990) 7119–7128.
[30] W.J. Pitz, C.K. Westbrook, Combust. Flame 63 (1986) 113–133.
[31] B. Ruscic, A.F. Wagner, L.B. Harding, R.L. Asher, D. Feller, D.A. Dixon, K.A. Peterson, Y. Song, X.M. Qian, C.Y. Ng, J.B. Liu, W.W. Chen, J. Phys. Chem. A 106 (11) (2002) 2727–2747.
[32] A. Burcat, B. Ruscic, Third Millennium Ideal Gas and Condensed Phase Thermochemical Database for Combustion, 2009. <http://garfield.chem.elte.hu/Burcat/burcat.html>.
[33] A.N. Pirraglia, J.V. Michael, J.W. Sutherland, R.B. Klemm, J. Phys. Chem. 93 (1989) 282–291.
[34] J.P. Hessler, J. Phys. Chem. A 102 (24) (1998) 4517–4526.
[35] D.L. Baulch, C.T. Bowman, C.J. Cobos, R.A. Cox, T. Just, J.A. Kerr, M.J. Pilling, D. Stocker, J. Troe, W. Tsang, R.W. Walker, J. Warnatz, J. Phys. Chem. Ref. Data 34 (3) (2005) 757–1397.
[36] W. Tsang, R.F. Hampson, J. Phys. Chem. Ref. Data 15 (1986) 1087–1280.
[37] B.A. Ellingson, D.P. Theis, O. Tishchenko, J. Zheng, D.G. Truhlar, J. Phys. Chem. A 111 (51) (2007) 13554–13566.
[38] R.R. Baldwin, D. Jackson, R.W. Walker, S.J. Webster, Trans. Faraday Soc. 63 (535P) (1967) 1676.
[39] J.V. Michael, M.-C. Su, J.W. Sutherland, J.J. Carroll, A.F. Wagner, J. Phys. Chem. A 106 (21) (2002) 5297–5313.
[40] Z.K. Hong, R.D. Cook, D.F. Davidson, R.K. Hanson, J. Phys. Chem. A 114 (18) (2010) 5718–5727.
[41] J. Troe, Combust. Flame 158 (4) (2011) 594–601.
[42] S.R. Sellevåg, Y. Georgievskii, J.A. Miller, J. Phys. Chem. A 113 (16) (2009) 4457–4467.
[43] H. Hippler, J. Troe, Chem. Phys. Lett. 192 (4) (1992) 333–337.
[44] N.K. Srinivasan, J.V. Michael, Int. J. Chem. Kinet. 38 (3) (2006) 211–219.
[45] S.R. Sellevåg, Y. Georgievskii, J.A. Miller, J. Phys. Chem. A 112 (23) (2008) 5085–5095.
[46] J. Michael, J.W. Sutherland, J. Phys. Chem 92 (1988) 2853–3857.
[47] K.-Y. Lam, D.F. Davidson, R.K. Hanson, Int. J. Chem. Kinet., (2013) in press.
[48] R.C. Oldenborg, G.W. Loge, D.M. Harradine, K.R. Winn, J. Phys. Chem. 96 (21) (1992) 8426–8430.
[49] Z.K. Hong, S.S. Vasu, D.F. Davidson, R.K. Hanson, J. Phys. Chem. A 114 (17) (2010) 5520–5525.
[50] N.K. Srinivasan, M.C. Su, J.W. Sutherland, J.V. Michael, B. Ruscic, J. Phys. Chem. A 110 (21) (2006) 6602–6607.
[51] L.F. Keyser, J. Phys. Chem. 92 (1988) 1193–1200.
[52] D.L. Baulch, C.J. Cobos, R.A. Cox, C. Esser, P. Frank, T. Just, J.A. Kerr, M.J. Pilling, J. Troe, R.W. Walker, J. Warnatz, J. Phys. Chem. Ref. Data 21 (3) (1992) 411–734.
[53] L.B. Harding, S.J. Klippenstein, personal communication.
[54] H. Hippler, J. Troe, J. Willner, J. Chem. Phys. 93 (3) (1990) 1755–1760.
[55] J.V. Michael, J.W. Sutherland, L.B. Harding, A.F. Wagner, Proc. Combust. Inst. 28 (2) (2000) 1471–1478.
[56] M. Ó Conaire, PhD Thesis, National University of Ireland Galway, 2005.
[57] M.A. Mueller, R.A. Yetter, F.L. Dryer, Int. J. Chem. Kinet. 31 (10) (1999) 705–724.
[58] P.R. Westmoreland, J.B. Howard, J.P. Longwell, A.M. Dean, AIChE J. 32 (12) (1986) 1971–1979.
[59] J. Troe, J. Phys. Chem. 83 (1979) 114–126.
[60] H. Sun, S.I. Yang, G. Jomaas, C.K. Law, Proc. Combust. Inst. 31 (1) (2007) 439–446.
[61] R.R. Baldwin, D. Jackson, A. Melvin, B.N. Rossiter, Int. J. Chem. Kinet. 4 (1972) 277–292.
[62] Z.W. Zhao, J. Li, A. Kazakov, F.L. Dryer, Int. J. Chem. Kinet. 37 (5) (2005) 282–295.
[63] A.V. Joshi, H. Wang, Int. J. Chem. Kinet. 38 (1) (2006) 57–73.
[64] X. You, H. Wang, E. Goos, C-J. Sung, S.J. Klippenstein, J. Phys. Chem. A 111 (19) (2007) 4031–4042.
[65] M. Chaos, F.L. Dryer, Combust. Sci. Technol. 180 (6) (2008) 1053–1096.
[66] C.-J. Sung, C.K. Law, Combust. Sci. Technol. 180 (6) (2008) 1097–1116.
[67] C.L. Rasmussen, J. Hansen, P. Marshall, P. Glarborg, Int. J. Chem. Kinet. 40 (8) (2008) 454–480.
[68] D.M. Kalitan, J.D. Mertens, M.W. Crofton, E.L. Petersen, J. Propuls. Power 23 (6) (2007) 1291–1303.

[69] K.A. Bhaskaran, M.C. Gupta, T. Just, Combust. Flame 21 (1) (1973) 45–48.
[70] J. Herzler, C. Naumann, Proc. Combust. Inst. 32 (1) (2009) 213–220.
[71] T. Kathrotia, M. Fikri, M. Bozkurt, M. Hartmann, U. Riedel, C. Schulz, Combust. Flame 157 (7) (2010) 1261–1273.
[72] M. Tamura, P.A. Berg, J.E. Harrington, J. Luque, J.B. Jeffries, G.P. Smith, D.R. Crosley, Combust. Flame 114 (3–4) (1998) 502–514.
[73] L. Brett, J. MacNamara, P. Musch, J.M. Simmie, Combust. Flame 124 (1–2) (2001) 326–329.
[74] S.M. Gallagher, H.J. Curran, W.K. Metcalfe, D. Healy, J.M. Simmie, G. Bourque, Combust. Flame 153 (1–2) (2008) 316–333.
[75] J. Würmel, J.M. Simmie, Combust. Flame 141 (2005) 417–430.
[76] Morley, Gaseq ver 0.79, 2005. <http://www.c.morley.dsl.pipex.com/>.
[77] G. Mittal, PhD Thesis, Case Western Reserve University, 2006.
[78] G. Mittal, C-J. Sung, Combust. Sci. Technol. 179 (2007) 497–530.
[79] A.K. Das, C.J. Sung, Yu Zhang, G. Mittal, Int. J. Hydrogen Energy 37 (2012) 6901–6911.
[80] V. Babushok, W. Tsanga, G.T. Linteris, D. Reinelt, Combust. Flame 115 (1998) 551–560.
[81] H.R. Ambler, T.C. Sutton, Analyst (1934) 809–811.
[82] J. Sendroy Jr., H.A. Collison, H.J. Mark, Anal. Chem. 27 (1995) 1641–1645.
[83] M.C. Krejci, O. Mathieu, A.J. Vissotski, S. Ravi, T.G. Sikes, E.L. Petersen, A. Keromnes, W. Metcalfe, H.J. Curran Paper GT2012-69290, Proceedings of ASME Turbo Expo 2012-GT2012.
[84] E.L. Petersen, M.J.A. Rickard, M.W. Crofton, E.D. Abbey, M.J. Traum, D.M. Kalitan, Meas. Sci. Technol. 16 (2005) 1716–1729.
[85] G.A. Pang, D.F. Davidson, R.K. Hanson, Proc. Combust. Inst. 32 (2009) 181–188.
[86] J. de Vries, W. Lowry, Z. Serinyel, H.J. Curran, E.L. Petersen, Fuel 90 (1) (2011) 331–338.
[87] W. Lowry, J. de Vries, M. Krejci, Z. Serinyel, W. Metcalfe, H.J. Curran, E.L. Petersen, G. Bourque, J. Eng. Gas Turb. Power 133 (9) (2011). Article Number: 091501..
[88] G.S. Settles, Schlieren and Shadowgraph Techniques, Springer, Heidelberg, Germany, 2006.
[89] J. Herzler, C. Naumann, Combust. Sci. Technol. 180 (2008) 2015–2028.
[90] J.W. Sutherland, J.V. Michael, A.N. Pirraglia, F.L. Nesbitt, R.B. Klemm, Proc. Combust. Inst. 21 (1986) 929–941.
[91] J.W. Sutherland, P.M. Patterson, R.B. Klemm, Proc. Combust. Inst. 23 (1991) 51–57.
[92] R.S. Timonen, E. Ratajczak, D. Gutman, J. Phys. Chem. 92 (3) (1988) 651–655.
[93] R.S. Timonen, E. Ratajczak, D. Gutman, J. Phys. Chem. 91 (3) (1987) 692–694.
[94] P.H. Paul, J.L. Durant, J.A. Gray, M.R. Furlanetto, J. Chem. Phys. 102 (21) (1995) 8378–8384.
[95] G.P. Smith, J. Luque, C. Park, J.B. Jeffries, D.R. Crosley, Combust. Flame 131 (1–2) (2002) 59–69.